Research Square

Preprints are preliminary reports that have not undergone peer review.
They should not be considered conclusive, used to inform clinical practice,
or referenced by the media as validated information.

Beyond Hosting Capacity: A Multidimensional Diagnostic for Renewable Integration in Low-Inertia Power Systems

Narciso Moreno-Alfonso

narciso-ma@us.es

University of Seville

Juan-Carlos Bravo-Rodriguez

University of Seville

Alfonso Bachiller-Soler

University of Seville

Research Article

Keywords: Renewable integration diagnostics, hosting capacity, low-inertia power systems, multidimensional composite index, transient stability, frequency stability

Posted Date: May 26th, 2026

DOI: https://doi.org/10.21203/rs.3.rs-9752003/v1

License: This work is licensed under a Creative Commons Attribution 4.0 International License.
Read Full License

Additional Declarations: No competing interests reported.

Beyond Hosting Capacity: A Multidimensional Diagnostic for Renewable Integration in Low-Inertia Power Systems

Narciso Moreno-Alfonso[1*], Juan-Carlos Bravo-Rodriguez[2] and Alfonso Bachiller-Soler[3]

[1,2,3*]Departamento de Ingeniería Eléctrica, Universidad de Sevilla, Avda. de los Descubrimientos, Sevilla, 41092, Sevilla, Spain.

*Corresponding author(s). E-mail(s): narciso-ma@us.es;

Abstract

Renewable penetration indicators quantify *how much* generation a power system integrates while remaining blind to *what* limits further integration and *where* that limitation originates. This paper introduces the *Multi-dimensional Renewable Integration Diagnostic* (MRID), to our knowledge the first dimensionless index that resolves both questions in a single computation. The MRID aggregates seven independently normalised sub-indices covering hosting capacity, inertia adequacy, transient stability, flexibility reserve, power quality, frequency nadir and grid strength. A weighted geometric mean combines them into a single score and prevents cross-dimensional masking. A spatial diagnostic layer comprising branch load indices, bus-level short-circuit ratios, inertial participation factors and a distributed-generation location benefit indicator names the network element responsible for the binding constraint. A five-level Integration Regime Type (IRT) classification anchored in international grid codes maps continuous MRID values to operationally actionable states and provides objective definitions for the otherwise qualitative notions of *low* and *high* renewable penetration. Validation on the IEEE 9-, 14-, 30- and 118-bus systems yields four principal findings: (i) the same scalar penetration places systems up to three regimes apart and the spatial layer names the responsible element; (ii) enabling technologies such as BESS and grid-forming inverters unlock integration capacity only in dynamically constrained systems and leave statically constrained ones essentially pinned; (iii) without case-specific tuning, the index reproduces on every benchmark the limiting mechanism that decades of independent literature have documented for it; and (iv) the diagnostic is robust to ± 0.10 weight perturbations, while a Monte Carlo benchmark against an electromechanical-restricted baseline isolates hosting capacity and grid strength as the irreducible information the MRID adds. The MRID thus operationalises in a single computation what previously required dispersed expert analysis, extending diagnostic capability to systems where comparable analysis is not yet available.

Keywords: Renewable integration diagnostics, hosting capacity, low-inertia power systems, multidimensional composite index, transient stability, frequency stability

1 Introduction

Regulatory bodies and the technical literature routinely refer to "high renewable penetration" without a unified operational definition: some authors rely on installed-capacity ratios (Strelkov and Strelkova 2020), others on energy-based metrics over given time periods (Yu et al. 2021),

and others on real-time demand-based indicators (Niu et al. 2022). This lack of consistency and methodological standardisation has practical impacts that are amplified by the rapid growth of variable renewable energy sources (VRES), which increases the need for consistent frameworks to characterise their systemic effects (Milano et al. 2018; Ratnam et al. 2020; Denholm et al. 2020).

In practice, this inconsistency leads to four direct consequences. First, and most critically, existing indices reveal *how much* renewable energy penetrates the system but not *why* that penetration degrades operation nor *where* the problem originates in the network topology, which is precisely the diagnostic dimension that operators need to design effective countermeasures. Second, it obscures the differential contribution of enabling technologies such as BESS, synthetic inertia, and active curtailment to the real integration capacity of the system. Third, it precludes the establishment of design thresholds transferable to system operators and regulators. Fourth, it prevents rigorous comparison across studies conducted on systems of different scale and topology.

Resolving these limitations requires a common reference for the penetration variable itself. Throughout this paper, λ denotes the instantaneous power penetration fraction, defined as the ratio of renewable generation to total demand. Section 2.1 reviews the alternative formulations and justifies this choice as the one that most directly couples the operating point to the dynamic and structural constraints that the index later quantifies.

The proposed **MRID** addresses the above limitations as a planned-operation hosting capacity index that assesses whether a system with characteristics $\boldsymbol{\xi}$ can operate securely under a renewable penetration λ. The index simultaneously quantifies seven independent physical constraints in a single dimensionless scalar MRID $\in [0, 1]$, computable from standard power system analysis tools (AC load flow, generator and storage models). Its formulation identifies not only the dominant constraint but also its network location, endowing the indicator with direct diagnostic capability.

The operational classification of the MRID into five Integration Regime Types (IRT, Section 4) carries a conceptual consequence that extends beyond the index itself: the terms "low" and "high" renewable penetration acquire an objective cross-system meaning. Two operators reporting that their systems run under "high penetration" may today describe substantially different operating regimes, since any conventional scalar penetration metric only counts megawatts and is silent on whether the system is comfortably hosting them or approaching a structural feasibility boundary. The MRID resolves this ambiguity by anchoring the qualifier to a quantifiable integration regime. A system in IRT-I or IRT-II hosts renewables in a structurally low-stress regime regardless of the numerical value of λ, while one in IRT-IV or IRT-V is in a high-stress regime even at moderate λ values that classical metrics would classify as safe. The MRID therefore reframes renewable penetration from a volume-based qualifier into an operational-state classification.

Section 6 characterises the diagnostic behaviour of the MRID through a baseline evaluation of MRID(λ) on the standard IEEE 9-, 14-, 30- and 118-bus systems, complemented by three thematic studies of discriminating capacity, technology enablers and limits, and robustness and uncertainty.

The contributions of this work are:

C1. Definition of a unified diagnostic index for renewable integration. The MRID is, to our knowledge, the first single dimensionless scalar that diagnoses integration capacity by jointly aggregating seven physically independent constraints from standard AC load-flow data. Its weighted geometric construction analytically guarantees that the binding constraint governs the global value without cross-dimensional compensation, a property no additive aggregation provides and the reason the index functions as a faithful diagnostic of the binding mechanism rather than a smoothed score.

C2. Discriminative identification of underlying integration regimes. The MRID maps the continuous scale into five Integration Regime Types (IRT) anchored in quantifiable international grid codes (ENTSO-E 2022), allowing operators to identify whether the binding factor is inertia, voltage support, network capacity, or stability margins,

instead of relying on aggregate penetration values that mask the underlying grid behaviour.

C3. Reproduction of expert diagnostic intuition by a single computation. Applied without case-specific calibration to the four standard IEEE benchmarks, the MRID identifies on each the same limiting mechanism that decades of independent literature have documented: frequency-stability margins for the 9- and 118-bus systems, voltage support at weak buses for the 30-bus system, and the combined voltage-support and grid-strength constraint for the 14-bus system. By collapsing this distributed body of expert analysis into a single computation, it provides the case-study basis for trusting its diagnosis in systems where comparable expert intuition does not yet exist.

C4. Network-element-level localisation of limiting constraints. The MRID transforms a single aggregate score into physically grounded, element-wise evidence that reveals the specific lines, buses or generators constraining admissibility, providing the actionable insight required for planning and operation. Four complementary spatial diagnostics covering thermal loading, short-circuit strength, inertial participation and distributed-generation siting support this localisation.

C5. Identification of diagnostic dimensions beyond electromechanical formulations. The MRID elevates hosting capacity and grid strength to first-class integration constraints, dimensions that purely electromechanical indices treat as exogenous. In network-constrained systems these dimensions, rather than stability margins, set the admissibility ceiling, and ignoring them produces an inflated and ultimately misleading estimate of integration capacity (Wang and Milanović 2024).

C6. Use of the MRID as a pre-contingency decision tool for planning and model-predictive control. The analytical differentiability of all seven sub-indices yields a closed-form gradient that turns the MRID into a cost function for MPC dispatch in low-inertia systems at the computational cost of an AC load flow. Section 7.5 demonstrates this use on two contrasting IEEE benchmarks.

2 Related Work

Existing approaches to renewable integration address isolated dimensions of the problem rather than its joint diagnosis. Voltage-reactive sensitivity formulations have been proposed for systems with increasing renewable penetration (Adetokun et al. 2020), but they do not incorporate dynamic or flexibility content. Operational flexibility metrics such as the "flexibility confidence capacity" (Bai et al. 2023) characterise the dispatch envelope without explicitly integrating transient stability or inertia adequacy. Stability analyses in low-inertia systems (Milano et al. 2018; Teng et al. 2016) provide a rigorous dynamic foundation but stop short of deriving penetration indices capable of evaluating integration capacity. At the system-operator level, the SNSP (Nedd et al. 2021) is the most widely adopted operational metric for high renewable penetration. Two systems with identical SNSP, however, can exhibit fundamentally different behaviour in frequency stability, flexibility and voltage robustness. A complementary line of work on hosting-capacity assessment (Benzerga et al. 2025; Mousa et al. 2024) concentrates on distribution networks and treats hosting capacity as a static threshold rather than as a system-wide operational constraint dependent on the operating point.

2.1 Renewable penetration definitions

No universally adopted metric exists for quantifying renewable penetration (Nejla et al. 2025). Definitions fall into two broad categories: *structural indicators*, which describe long-term system composition, and *operational indicators*, which capture real-time state.

Under any of these metrics, a system with high penetration but severe curtailment and degraded voltages receives the same index value as one with full integration (Nedd et al. 2021). None captures network constraints or integration quality, nor enables comparison across systems of different

scale. These limitations are the primary motivation for the MRID, and Table 1 reports the complete comparative analysis.

2.1.1 Instantaneous power penetration

This metric is most relevant for stability assessment because it corresponds to periods of highest network control stress:

$$\lambda_P = \frac{P_{\text{RES}}(t)}{P_{\text{load}}(t)}, \quad \lambda_P \in [0, \infty) \tag{1}$$

where P_{RES} is the power injected by renewable sources and P_{load} the total demand.

A widely used operational variant is the System Non-Synchronous Penetration (SNSP) ratio, defined as (EirGrid 2025):

$$\text{SNSP}(t) = \frac{P_{\text{IBR}}(t) + P_{\text{import}}(t)}{P_{\text{load}}(t) + P_{\text{export}}(t)} \tag{2}$$

where P_{IBR} is the power from inverter-based resources (IBR), P_{import} the asynchronous imported power, and the denominator represents total net demand. The SNSP extends λ_P by explicitly accounting for asynchronous power exchanges, making it particularly representative in highly interconnected systems. Ireland's operational SNSP limit was raised to 75 % in 2022, with a roadmap to 95 % by 2030 through grid-forming inverters and increased HVDC interconnection (EirGrid 2025). Similar frequency-stability-based operational limits have been adopted by other system operators (AEMO 2022; ENTSO-E; ESO 2021; Energinet 2019), though typically as decoupled metrics rather than unified synthetic indices.

In this work, the instantaneous penetration λ_P is adopted as the reference variable, as it directly characterises the operating point of the system under planned conditions. The SNSP is not used as the primary benchmark in the present analysis, since the evaluation frameworks defined for the standard test systems do not include asynchronous imports or exports.

2.1.2 Renewable energy coverage

The ratio of total renewable energy generated to total energy consumed in a given period provides the reference metric for medium- and long-term planning and decarbonisation tracking. However, by averaging temporal variability over the computation horizon, it conceals extreme operating episodes governing system stability, particularly high instantaneous penetration events and frequency transients (Yu et al. 2021; Nejla et al. 2025).

2.1.3 Installed capacity penetration

The ratio of installed renewable capacity C_{RES} [MVA] to total generation capacity C_{total} is (Strelkov and Strelkova 2020; Yu et al. 2021):

$$\lambda_C = \frac{C_{\text{RES}}}{C_{\text{total}}} = \frac{C_{\text{RES}}}{C_{\text{RES}} + C_{\text{conv}}} \tag{3}$$

where C_{conv} [MVA] is the installed conventional capacity. This static indicator is relevant for transmission planning and long-term scenario analysis but carries no information about instantaneous operating state.

2.2 Hosting capacity

A unified Hosting Capacity (HC) definition covering different distributed energy resource (DER) types, analysis horizons, and methodological approaches has been proposed in (Benzerga et al. 2025). A recent survey of HC methods for active distribution networks (Mousa et al. 2024) identifies a clear trend towards data-driven and machine-learning approaches. Both treat HC primarily as a structural property of the network, a framing that the present paper extends to a system-wide operational reading in Section 3.3.

2.3 Frequency stability indicators

Frequency stability is one of the most critical operational concerns in systems with high IBR penetration. RoCoF and frequency nadir constraints are *independent* (Liu et al. 2024): a system can satisfy the instantaneous RoCoF limit while violating the nadir if the primary frequency response is insufficient or delayed. None of the three standard frequency security metrics in isolation, namely total synchronous inertia H_{sys}, post-event RoCoF, and frequency nadir, is sufficient to characterise system security (Nedd et al. 2021), which motivates integrated indicators that account jointly for effective inertia and

dynamic frequency response rather than relying on penetration-based scalars such as λ_P or SNSP.

2.4 Grid strength and IBR stability

Grid strength, commonly quantified through the Short-Circuit Ratio (SCR), is a key indicator in systems with high penetration of inverter-based resources (IBR). Grid-following (GFL) controls become unstable at SCR < 3 due to interactions between phase-locked loops (PLL) and the network (Rosso et al. 2021), a threshold adopted by ENTSO-E and IEC 61400-21 as a minimum reference level; grid-forming (GFM) controls exhibit greater robustness in the same low-SCR regime.

2.5 Stability indicators for increasing renewable penetration

Displacing synchronous generation with IBR reduces the equivalent system inertia, characterised by (Kundur 1994):

$$H_{\text{sys}}(\lambda) = \frac{\sum_{g \in \mathcal{G}_s(\lambda)} H_g S_g^{\text{rated}}}{S_{\text{tot}}^{\text{installed}}} \tag{4}$$

where $\mathcal{G}_s(\lambda)$ is the set of synchronous generators online at penetration λ, H_g their individual inertia constants [s], S_g^{rated} their rated apparent power [MVA], and $S_{\text{tot}}^{\text{installed}}$ the total installed capacity. The reduction in H_{sys} increases the Rate of Change of Frequency (RoCoF) following loss of a generating unit of power ΔP:

$$\left.\frac{df}{dt}\right|_{t=0^+} = -\frac{\Delta P \cdot f_0}{2\, H_{\text{sys}}\, S_{\text{tot}}} \tag{5}$$

where f_0 is the nominal frequency [Hz]. European network codes set RoCoF limits typically in the range $[0.5\text{–}2]\,\text{Hz}\,\text{s}^{-1}$ (ENTSO-E 2022; EC 2016).

Recent literature has analysed the impact of GFL/GFM fleet composition on transient stability in converter-dominated systems, proposing extended equal-area criteria, energy function methods, and phasor-based voltage stability indices for mixed GFL/GFM/synchronous fleets (Cai et al. 2024; Alizadeh and Sun 2025; Yang et al. 2025). However, these approaches are typically tailored to specific control strategies or operating scenarios, which limits their integration into aggregate, system-level diagnostic frameworks.

2.6 Composite indices

The most direct composite-index precedents (Nikolaidis et al. 2013; Ochoa et al. 2006) combine multi-dimensional performance indicators through weighted aggregation to assess DG integration, evaluated on the IEEE 9-bus and IEEE 34-bus feeder respectively. However, these approaches do not incorporate dynamic constraints such as RoCoF, CCT or frequency nadir, nor do they enforce strict dimensionless formulations or provide classification thresholds grounded in operational standards.

The closest multi-domain precedent (Wang and Milanović 2024) combines voltage, frequency, and angle stability criteria within a composite index and constitutes the most advanced aggregation effort to date. It nevertheless covers only a subset of system dimensions, omitting hosting capacity, grid strength, power quality and operational flexibility, and depends on computationally expensive time-domain simulations rather than steady-state formulations. It also lacks spatial diagnostic capability and operational classification, both of which are essential for translating an aggregate score into network-level decisions.

Probabilistic stability analysis (Milanović 2017) derives distributions of frequency nadir and RoCoF through repeated simulation ($\sim 10^3$ runs), explicitly capturing uncertainty but at a high computational cost. This motivates the need for computationally efficient formulations capable of incorporating uncertainty within integrated assessment frameworks.

A correlation-regression analysis of short-circuit current, CCT, and RoCoF in wind-dominated systems (El Wejhani et al. 2025) reveals a fundamental trade-off: increased short-circuit strength improves transient stability margins while amplifying RoCoF. This result highlights the inherently multidimensional nature of system stability, where different constraints may evolve in opposing directions, requiring aggregation strategies capable of preserving the influence of the dominant limiting factor.

The concept of *network dynamic flexibility* (Brahma and Senroy 2021) further emphasises the importance of distinguishing between local and system-wide stability effects. This perspective supports the development of integration indices that combine global assessment with spatially resolved diagnostics, enabling the identification of location-dependent constraints within the network.

2.7 Research gaps and positioning

The advances reviewed above cover relevant dimensions in isolation, but none provides a unified framework capable of integrating physical diagnostics, penetration capacity and spatial localisation of the active constraint. The review identifies five critical gaps that the MRID addresses directly, as documented in Table 1:

(i) No existing index simultaneously integrates HC, RoCoF, nadir, CCT, flexibility reserve, power quality, and grid strength in a single normalised dimensionless scalar with spatial diagnostic capability.
(ii) Frequency nadir and RoCoF are routinely treated as equivalent constraints despite being physically independent.
(iii) Grid strength (SCR/WSCR) is seldom incorporated into general penetration indicators despite its operational relevance for IBR.
(iv) No penetration classification thresholds exist that are anchored in quantifiable international operational standards (ENTSO-E, IEC) and enable cross-system comparison.
(v) Existing penetration metrics lack the ability to localise limiting constraints and distinguish between fundamentally different integration regimes under identical penetration levels.

3 Formulation of the MRID

3.1 Design Principles

The MRID is designed around five core principles:

P1 – Dimensionlessness. The index and all sub-indices must lie in $[0, 1]$, where 1 denotes perfect integration with no active constraint and 0 denotes absolute infeasibility.
P2 – Dominant-constraint sensitivity. Saturation of any individual sub-index must degrade the global index significantly, preventing artificial cross-dimensional compensation.
P3 – Differentiability. Each sub-index must be differentiable with respect to system parameters to support sensitivity analysis and design gradients.
P4 – Computability from standard data. The formulation must be computable from AC load flow data and the generator and storage parameters routinely available in power system studies.
P5 – Monotonicity in λ of the aggregate index. For a fixed network, $\mathrm{MRID}(\lambda, \boldsymbol{\xi})$ must be non-increasing in λ, guaranteeing the existence of a maximum admissible penetration level λ^*.

3.2 MRID Structure

The MRID is defined as the weighted geometric mean of seven sub-indices:

$$\mathrm{MRID}(\lambda, \boldsymbol{\xi}) = \prod_{k \in \mathcal{K}} \Phi_k(\lambda, \boldsymbol{\xi})^{w_k} \qquad (6)$$
$$\mathcal{K} = \{HC, IA, TS, FR, PQ, NA, GS\}$$

where $w_k > 0$, $\sum_{k \in \mathcal{K}} w_k = 1$ are the weights, and $\lambda \in [0, 1]$ is the instantaneous penetration level defined in (1). The system parameter vector $\boldsymbol{\xi}$ encodes network topology, generator and BESS parameters, and load level.

Geometric aggregation is the natural choice for a multi-constraint integration index: any sub-index approaching zero drives MRID $\to 0$ regardless of the others, so the binding constraint governs the global value without cross-dimensional masking. The analytical sensitivity

$$\frac{\partial \mathrm{MRID}}{\partial w_k} = \mathrm{MRID} \cdot \ln(\Phi_k) \qquad (7)$$

identifies the binding sub-indices by sign, underpins the weight-perturbation check used in the robustness analysis later in the paper, and supplies the gradient required when the MRID is used as a cost function in planning or

Table 1 Comparison of the MRID against leading indicators in the literature. Column legend. Seven proposed dimensions: HC hosting capacity, IA inertia and RoCoF, TS transient stability and CCT, FR flexibility reserve, PQ power quality, NA frequency nadir, GS grid strength and SCR. Additional columns: Dim. dimensionless, Cls. normalised classification, Spa. spatial diagnostics. Coverage marks: ✓ covered, ○ partially, — not covered.

Work	HC	IA	TS	FR	PQ	NA	GS	Dim.	Cls.	Spa.
λ_E, λ_C (Strelkov and Strelkova 2020; Yu et al. 2021; Ríos-Ocampo et al. 2021)	—	—	—	—	—	—	—	○	—	—
SNSP (Nedd et al. 2021)	—	○	—	—	—	—	—	✓	—	—
HC analysis (Benzerga et al. 2025; Mousa et al. 2024; Keane and O'Malley 2005)	✓	—	—	—	○	—	—	○	—	○
VSI (FVSI, L-index) (Adetokun et al. 2020; Niu et al. 2022)	○	—	—	—	—	—	—	✓	—	—
Composite index (Nikolaidis et al. 2013)	○	—	—	—	○	—	—	○	—	—
DG index (Ochoa et al. 2006)	✓	—	—	—	○	—	—	○	—	—
Flex. confidence (Bai et al. 2023)	—	—	—	✓	—	—	—	○	—	—
Nadir-UC (Liu et al. 2024)	—	○	—	—	—	✓	—	—	—	—
GFM/SCR (Rosso et al. 2021)	—	—	—	—	—	—	✓	—	—	—
Reliability (Beyza and Yusta 2021; Ratnam et al. 2020)	—	○	○	○	—	—	—	○	—	—
Prob. multi-domain (Wang and Milanović 2024)	—	○	✓	—	—	✓	—	✓	—	—
Prob. stability analysis (Milanović 2017)	—	○	✓	—	—	○	—	○	—	—
Corr. I_{cc}-CCT-RoCoF (El Wejhani et al. 2025)	—	○	○	—	—	—	○	—	—	—
Inertia spatial distrib. (Brahma and Senroy 2021)	—	○	—	—	—	—	—	—	—	○
MRID (this work)	✓	✓	✓	✓	✓	✓	✓	✓	✓	✓

MPC schemes (Papadopoulos and Milanović 2017; Milanović 2017).

Table 2 lists the seven sub-indices and their default weights w_k^*. The default weights follow three criteria, namely operational severity, actuation time horizon, and available controllability:

$w_{HC} = w_{TS} = 0.20$. Hosting capacity and transient stability represent the most critical constraints, whose violation can immediately trigger protection actions such as generator disconnection or load shedding.

$w_{IA} = w_{FR} = 0.15$. Inertia adequacy and flexibility reserve act on a seconds-to-minutes horizon. Although their degradation affects stability, corrective actions are typically available before reaching critical conditions.

$w_{PQ} = w_{NA} = w_{GS} = 0.10$. Power quality, frequency nadir, and grid strength generally provide larger regulatory margins and can be mitigated through lower-cost control actions such as reactive power support or inverter regulation.

$\sum_k w_k = 1$. Normalisation ensures comparability across scenarios and preserves the bounded, dimensionless nature of the MRID.

For active distribution networks, w_{HC} and w_{PQ} should be increased at the expense of w_{IA} and w_{TS}, as follows from the weight sensitivity analysis (Section 7.4): transient stability becomes less critical in distribution systems with fast protection, while hosting capacity becomes the primary constraint (Benzerga et al. 2025; Mousa et al. 2024).

Each sub-index is defined in the following subsections, including its formulation, physical interpretation, and role within the MRID.

Table 2 MRID sub-indices, physical interpretation, and default weights for low-inertia systems.

Φ_k	Name	Dominant constraint	w_k^*
Φ_{HC}	Hosting Capacity	Voltage N-1, thermal loading	0.20
Φ_{IA}	Inertia Adequacy	RoCoF limit (ENTSO-E)	0.15
Φ_{TS}	Transient Stability	CCT vs. protection clearing time	0.20
Φ_{FR}	Flexibility Reserve	Reserve for renewable variability	0.15
Φ_{PQ}	Power Quality	Voltage profile, Δf	0.10
Φ_{NA}	Frequency Nadir	Nadir limit f_{nadir} (ENTSO-E)	0.10
Φ_{GS}	Grid Strength (WSCR)	WSCR $\geq$ SCR$_{\text{ref}}$	0.10

3.3 Hosting Capacity Sub-Index (Φ_{HC})

Hosting capacity is classically defined as the maximum renewable generation that can be injected without violating steady-state voltage limits or branch thermal ratings under the worst N-1 contingency, a static network characteristic evaluated at predefined locations. The sub-index Φ_{HC} adopted here turns this static bound into an operational proximity-to-limits indicator that depends on both the penetration level and the spatial distribution of injections, making hosting capacity an active constraint suitable for the optimal allocation of renewable generation as a planning task.

The global voltage violation index is defined as:

$$V_{\text{viol}}(\lambda) = \frac{1}{N_b} \cdot \sum_{i=1}^{N_b} \max\left(0,\ \frac{\left|V_i(\lambda) - V_{\text{nom}}\right| - \Delta V_{\max}}{\Delta V_{\max}}\right) \tag{8}$$

where $V_i(\lambda)$ is the bus voltage from the AC load flow at penetration λ, $V_{\text{nom}} = 1.0\,\text{pu}$, and $\Delta V_{\max}$ is the maximum admissible deviation, with a typical transmission value of $0.05\,\text{pu}$. The thermal loading violation index is defined analogously:

$$L_{\text{viol}}(\lambda) = \frac{1}{N_l} \sum_{l=1}^{N_l} \max\left(0,\ \frac{S_l(\lambda) - S_l^{\max}}{S_l^{\max}}\right) \tag{9}$$

where $S_l(\lambda)$ is the apparent power on branch l and $S_l^{\max}$ its thermal limit. The sub-index is then obtained via a saturating exponential penalty:

$$\Phi_{HC}(\lambda) = \exp\Big(-\mu_{HC}\left[V_{\text{viol}}(\lambda) + L_{\text{viol}}(\lambda)\right]\Big) \tag{10}$$

where $\mu_{HC} > 0$ is the stiffness parameter (default $\mu_{HC} = 10$). The exponential form ensures differentiability throughout the domain (principle P3) and satisfies $\Phi_{HC} \in (0, 1]$, with $\Phi_{HC} = 1$ when no violations are present and $\Phi_{HC} \to 0$ under severe violations.

3.4 Inertia Adequacy Sub-Index (Φ_{IA})

The system inertia $H_{\text{sys}}(\lambda)$ is computed via (4), where the set $\mathcal{G}_s(\lambda)$ includes only synchronous generators that inject active power. A synchronous machine dispatched to $P = 0$ but remaining connected as a synchronous condenser continues to contribute to H_{sys}, since its rotating mass remains coupled to the system. In the MRID formulation this contribution is captured as additional virtual inertia via the parameter H_{virt} of equation (13). The discriminating-capacity study defined in Section 6.3 quantifies this effect for the IEEE benchmark systems through dedicated synchronous-condenser and grid-forming full-fleet configurations.

As λ increases, disconnected synchronous generators cease to contribute to H_{sys}, reducing total effective inertia. The severity of the worst N-1 contingency depends on the generator dispatch mix at each penetration level:

$$\Delta P_{\max}(\lambda) = \max\left(\frac{(1-\lambda)\,P_{\text{load}}}{n_s(\lambda)},\ \lambda\,P_{\text{load}}\right) \tag{11}$$

where $n_s(\lambda)$ is the number of synchronous generators online at penetration λ. The first term is the loss of the largest individual synchronous unit; the second is the loss of the entire IBR plant when it is concentrated at few buses. For

$\lambda \gtrsim 0.55$ as parameterised in the IEEE 9-bus system, the renewable plant becomes the dominant contingency. The minimum inertia required to satisfy the RoCoF limit under this contingency is obtained by solving (5) for H_{sys}:

$$H_{\min}^{\text{RoCoF}} = \frac{f_0 \, \Delta P_{\max}}{2 \, S_{\text{tot}} \, \dot{f}_{\max}} \tag{12}$$

where $\dot{f}_{\max}$ is the RoCoF limit [Hz/s]. The BESS contribution to virtual inertia (synthetic inertia) is modelled as additional equivalent inertia:

$$H_{\text{virt}}(\lambda) = \frac{P_{\text{BESS}}^{\text{cap}} \, \tau_{\text{BESS}}}{2 \, S_{\text{tot}}^{\text{installed}}} \tag{13}$$

where $P_{\text{BESS}}^{\text{cap}}$ is the BESS rated power [MW] and τ_{BESS} is the synthetic inertia control time constant [s]. When the IBR fleet includes a fraction $k_{\text{GFM}} \in [0, 1]$ of grid-forming inverters, these contribute distributed virtual inertia that partially recovers the synchronous inertia displaced by renewable penetration:

$$H_{\text{GFM}}(\lambda) = k_{\text{GFM}} \, \max\!\big(0, \; H_{\text{sys}}^{0} - H_{\text{sys}}(\lambda)\big) \tag{14}$$

where H_{sys}^{0} is the synchronous inertia of the baseline fleet at $\lambda = 0$. The total effective inertia is then the sum of the residual synchronous inertia, the BESS synthetic inertia and the GFM virtual inertia:

$$H_{\text{eff}}(\lambda) = H_{\text{sys}}(\lambda) + H_{\text{virt}}(\lambda) + H_{\text{GFM}}(\lambda) \tag{15}$$

In the baseline case without GFM inverters ($k_{\text{GFM}} = 0$), $H_{\text{GFM}} = 0$ and the expression reduces to the classical sum of synchronous and BESS synthetic inertia. The inertia adequacy sub-index is then defined as

$$\Phi_{IA}(\lambda) = \min\!\left(1, \; \frac{H_{\text{eff}}(\lambda)}{H_{\min}^{\text{RoCoF}}}\right) \tag{16}$$

This formulation is linear in H_{eff}, facilitating gradient computation in sensitivity analysis.

3.5 Transient Stability Sub-Index (Φ_{TS})

The transient stability sub-index quantifies the dynamic security margin against three-phase faults at the most critical bus. For the OMIB equivalent of the system at penetration λ, the pre-fault rotor angle is

$$\delta_0(\lambda) = \arcsin\!\left(\frac{P_m}{E' \, V_\infty / X_d'(\lambda)}\right) \tag{17}$$

where E' is the internal voltage of the equivalent generator, V_∞ the infinite-bus voltage, $X_d'(\lambda)$ the equivalent transient reactance, which depends on λ through generator commitment and decommitment, and P_m the mechanical power of the OMIB equivalent. The critical clearing angle is obtained from the equal-area criterion:

$$\delta_{\text{cr}}(\lambda) = \pi - \arcsin\!\left(\frac{P_m - P_{e,\text{post}}^{\text{offset}}(\lambda)}{P_{e,\max,\text{post}}(\lambda)}\right) \tag{18}$$

where $P_{e,\max,\text{post}}(\lambda)$ is the maximum transferable electrical power in the post-fault topology and $P_{e,\text{post}}^{\text{offset}}$ is the power-axis offset due to transfer conductances. Integrating the equal-area criterion under the assumption of a three-phase fault ($P_{e,\text{fault}} \approx 0$) yields the analytical critical clearing time:

$$\text{CCT}(\lambda) = \sqrt{\frac{2 \, H_{\text{OMIB}} \big(\delta_{\text{cr}}(\lambda) - \delta_0(\lambda)\big)}{\pi \, f_0 \, P_m}} \tag{19}$$

where H_{OMIB} is the inertia constant of the critical generator (the lowest-H unit on line) and f_0 is the nominal frequency. The reactance $X_d'(\lambda)$ entering δ_0 and δ_{cr} is recomputed at each penetration level from the bus admittance matrix, so that CCT responds both to commitment changes and to topological perturbations such as the impedance scaling examined in the discriminating-capacity study of Section 6.3.

As penetration increases, the synchronising torque available from the residual synchronous fleet decreases and the post-fault stability margin shrinks. This effect is captured by the synchronising torque support factor

$$\begin{aligned} f_{\text{syn}}(\lambda) &= \sqrt{(1 - \lambda) + k_{\text{GFM}} \, \lambda} \\ &= \sqrt{1 - (1 - k_{\text{GFM}}) \, \lambda} \end{aligned} \tag{20}$$

which equals $\sqrt{1 - \lambda}$ for a purely GFL fleet and approaches unity as $k_{\text{GFM}} \to 1$, since GFM

inverters partially restore the synchronising contribution that GFL inverters lack. The sub-index is then defined relative to a reference clearing time $\mathrm{CCT}_{\mathrm{ref}}$, set to the maximum back-up protection relay actuation time of 0.250 s, equivalent to 15 cycles at 60 Hz:

$$\Phi_{TS}(\lambda) = \min\left(1,\ f_{\mathrm{syn}}(\lambda)\,\frac{\mathrm{CCT}(\lambda)}{\mathrm{CCT}_{\mathrm{ref}}}\right) \tag{21}$$

At $\lambda = 1$ with $k_{\mathrm{GFM}} = 0$ the factor f_{syn} vanishes, reflecting complete loss of synchronising torque. Whenever $\mathrm{CCT}(\lambda)\, f_{\mathrm{syn}}(\lambda) < \mathrm{CCT}_{\mathrm{ref}}$, the system cannot clear the fault before losing synchronism and $\Phi_{TS} < 1$ penalises the global index in proportion to the margin deficit. The analytical CCT derived from the OMIB model in (19) provides a criterion equivalent to time-domain transient stability indices (Papadopoulos and Milanović 2017) at the computational cost of an AC load flow, making it directly compatible with principles P3 and P4 outlined in Section 3.1.

3.6 Flexibility Reserve Sub-Index (Φ_{FR})

The available flexibility reserve $R_{\mathrm{av}}(\lambda)$ represents the total system capacity to respond to power imbalances on short time horizons. It is modelled as the sum of three main contributions: the headroom of online synchronous generators, the immediate discharge capacity of storage, and the fast frequency response of converter-based resources:

$$R_{\mathrm{av}}(\lambda) = R_{\mathrm{sync}}(\lambda) + R_{\mathrm{BESS}}(\lambda) + R_{\mathrm{FFR}}(\lambda) \tag{22}$$

where each term is defined as:

$$R_{\mathrm{sync}}(\lambda) = \sum_{g \in \mathcal{G}_s(\lambda)} \left(P_g^{\max} - P_g(\lambda)\right) \tag{23}$$

$$R_{\mathrm{BESS}}(\lambda) = P_{\mathrm{BESS}}^{\mathrm{cap}} \cdot \mathrm{SoC}(\lambda) \tag{24}$$

$$R_{\mathrm{FFR}}(\lambda) = \eta_{\mathrm{FFR}}\, P_{\mathrm{IBR}}(\lambda) \tag{25}$$

where $\mathcal{G}_s(\lambda)$ is the set of synchronous generators in service at penetration λ, $P_g^{\max}$ is the rated power of generator g, and $P_g(\lambda)$ its dispatch setpoint. The BESS rated power is $P_{\mathrm{BESS}}^{\mathrm{cap}}$, $\mathrm{SoC}(\lambda) \in [0,1]$ is its available state of charge, $\eta_{\mathrm{FFR}} \in [0,1]$ is the fraction of converter-based power available as fast frequency response, and $P_{\mathrm{IBR}}(\lambda) = \lambda\, P_{\mathrm{load}}$ is the total power injected by IBR resources.

The reserve requirement $R_{\mathrm{req}}(\lambda)$ is defined as the sum of a component associated with renewable generation variability and the largest generation loss under the N-1 criterion:

$$R_{\mathrm{req}}(\lambda) = k_R\, P_{\mathrm{RES}}^{\mathrm{av}}(\lambda) + \Delta P_{\max} \tag{26}$$

The coefficient $k_R \in [0.1, 0.2]$ represents the fraction of renewable power that must be backed up to absorb short-horizon fluctuations. This deterministic parameter admits a direct probabilistic interpretation: if renewable generation is modelled as a normally distributed random variable with mean $P_{\mathrm{RES}}^{\mathrm{av}}$ and coefficient of variation CV, the reserve requirement for a confidence level α is

$$R_{\mathrm{req}}^{(\alpha)} = z_\alpha\, \mathrm{CV}\, P_{\mathrm{RES}}^{\mathrm{av}} + \Delta P_{\max},$$

where $z_\alpha = \Phi^{-1}(\alpha)$ is the standard normal quantile. The reference value $k_R = 0.15$ corresponds to a 95% confidence level and CV ≈ 0.09, characteristic of solar generation on 15-minute horizons (Bai et al. 2023). Higher CV values, typical of wind generation in the $[0.15, 0.20]$ range, imply proportionally larger reserve requirements; lower values, typical of solar in the $[0.08, 0.12]$ range, lead to more moderate requirements, and k_R can be recalibrated accordingly for any given renewable technology mix.

The flexibility reserve sub-index is defined as:

$$\Phi_{FR}(\lambda) = \min\left(1,\ \frac{R_{\mathrm{av}}(\lambda)}{R_{\mathrm{req}}(\lambda)}\right) \tag{27}$$

$\Phi_{FR} = 1$ corresponds to available reserve covering both renewable variability and the worst N-1 contingency; $\Phi_{FR} < 1$ flags a flexibility deficit.

3.7 Power Quality Sub-Index (Φ_{PQ})

The power quality sub-index integrates static voltage deviation and quasi-steady-state frequency deviation into a single component:

$$\Phi_{PQ}(\lambda) = \Phi_V^{\alpha_V}(\lambda) \cdot \Phi_f^{\alpha_f}(\lambda), \quad \alpha_V + \alpha_f = 1 \tag{28}$$

where the individual components are

$$\Phi_V(\lambda) = 1 - \frac{1}{N_b} \sum_{i=1}^{N_b} \frac{|V_i(\lambda) - 1|}{\Delta V_{\max}} \tag{29}$$

$$\Phi_f(\lambda) = 1 - \frac{\sigma_f(\lambda)}{\Delta f_{\max}} \tag{30}$$

with $\sigma_f(\lambda)$ the standard deviation of frequency over the operating horizon and $\Delta f_{\max} = 0.2\,\text{Hz}$ the admissible deviation in normal operation. Both components are clipped to $[0, 1]$ via $\max(0, \cdot)$.

3.8 Frequency Nadir Sub-Index (Φ_{NA})

The frequency nadir f_{nadir} is the minimum absolute frequency reached after the loss of the largest generator, once inertia has slowed the initial decline but before the governor achieves full response. Unlike the RoCoF, which limits the initial rate of frequency decline, the nadir depends on the integral of the frequency trajectory until the governor acts fully. Consequently, systems with similar H_{eff} but different governor response times τ_g can exhibit very different nadirs. The nadir constraint is therefore independent of the RoCoF constraint (ENTSO-E 2022; Denholm et al. 2020; Liu et al. 2024).

Using a first-order model with load damping correction, the nadir is upper-bounded by:

$$f_{\text{nadir}}(\lambda) \approx f_0 - \frac{f_0\,\Delta P_{\max}\,\tau_g}{2\,H_{\text{eff}}(\lambda)\,S_{\text{tot}}} + \frac{D_{\text{load}}^{\text{pu}}\,P_{\text{load}}\,\tau_g}{2\,S_{\text{tot}}} \tag{31}$$

where τ_g [s] is the governor response time, typically 2 to 5 s for steam turbines, $\Delta P_{\max}$ is the largest N-1 generation loss, and $D_{\text{load}}^{\text{pu}} \approx 0.015$ is the load damping coefficient as defined in standard power-system practice (Kundur 1994). The second term is the positive correction from load damping, which reduces the pessimistic bias of the zero-order classical model. For the IEEE transmission systems analysed here this correction is below 0.01 Hz, yet preserves the correct physical sign and eliminates systematic overestimation of the nadir deficit.

ENTSO-E sets the minimum frequency security threshold of $f_{\text{nadir,min}} = 49.0\,\text{Hz}$ for the Continental European synchronous area. The sub-index is normalised between this limit and the nominal frequency:

$$\Phi_{NA}(\lambda) = \min\left(1,\ \frac{f_{\text{nadir}}(\lambda) - f_{\text{nadir,min}}}{f_0 - f_{\text{nadir,min}}}\right) \tag{32}$$

with $\Phi_{NA} = 1$ when the frequency nadir remains close to nominal conditions and $\Phi_{NA} = 0$ when $f_{\text{nadir}} \le f_{\text{nadir,min}}$. Although Φ_{NA} and Φ_{IA} both depend on H_{eff}, they capture distinct phenomena: Φ_{IA} limits the *rate* of frequency decline, while Φ_{NA} constrains the *absolute minimum frequency* reached after a disturbance. The governor response time τ_g, which appears explicitly in (31) and is calibrated by machine type, together with the load damping correction $D_{\text{load}}^{\text{pu}}$, constitute the dynamic parameters incorporated in the adopted first-order model.

3.9 Grid Strength Sub-Index (Φ_{GS})

Converter-based renewable sources (IBR) require sufficiently low network impedance at their point of connection to maintain phase-locked-loop (PLL) stability and current control (Rosso et al. 2021). This characteristic is quantified by the Short-Circuit Ratio (SCR).

$$\begin{aligned} \text{SCR}_i &= \frac{S_{\text{cc},i}}{P_{\text{RES},i}} \\ S_{\text{cc},i} &\approx \frac{V_{\text{nom}}^2}{|Z_{\text{th},i}|} = V_{\text{nom}}^2\,|Y_{\text{bus}}(i,i)| \end{aligned} \tag{33}$$

where $Z_{\text{th},i}$ is the Thévenin impedance at bus i, approximated by the reciprocal of the diagonal admittance $Y_{\text{bus}}(i,i)$. This expression yields a conservative estimate of S_{cc} that remains valid for relative comparison across scenarios.

In systems with multiple renewable plants, their interaction can degrade the effective grid strength below the individual bus SCR. The Weighted Short-Circuit Ratio (WSCR) is adopted, which weights the SCR of each bus by the square of the injected power, giving greater influence to the largest plants that dominate local

stability (NERC 2017):

$$\mathrm{WSCR}(\lambda) = \frac{\sum_{i \in \mathcal{B}_{\mathrm{RES}}} \mathrm{SCR}_i(\lambda)\, P^2_{\mathrm{RES},i}(\lambda)}{\sum_{i \in \mathcal{B}_{\mathrm{RES}}} P^2_{\mathrm{RES},i}(\lambda)} \tag{34}$$

where $\mathcal{B}_{\mathrm{RES}}$ is the set of buses with IBR generation. The grid strength sub-index is then defined as:

$$\Phi_{GS}(\lambda) = \min\left(1,\ \frac{\mathrm{WSCR}(\lambda)}{\mathrm{SCR}_{\mathrm{ref}}}\right) \tag{35}$$

with $\mathrm{SCR}_{\mathrm{ref}} = 3.0$ per IEC 61400-21. The power-squared weighting is more conservative than a simple average and better reflects current system-operator practice.

The sub-index Φ_{GS} captures the phenomenon commonly referred to as "weak grid": as λ increases and IBR generation occupies a growing fraction of the power installed at buses with low S_{cc} (ends of long lines, distribution-connected plants), WSCR decreases and Φ_{GS} penalises the global MRID even when the static load flow shows no appreciable voltage violations.

4 Integration Regime Types Classification

From the individual sub-indices and the composite MRID, five **Integration Regime Types** (IRT) are established. The five regimes and their thresholds are summarised in Table 3.

Five regimes are the minimal granularity that preserves operational interpretability without falling below the propagated MRID uncertainty of ±3 % under ±0.10 weight perturbations; three regimes would collapse the distinct limiting mechanisms that the case-study analysis of Section 7 later documents on the four benchmarks, and seven or more produce boundary widths statistically indistinguishable from this uncertainty. The chosen levels align with the planning lexicon *unconstrained*, *minor advisory*, *active operational measures*, *critical* and *inadmissible*.

Table 3 MRID Integration Regime Types (IRT) classification.

IRT	MRID range	Typical λ	Operational description
I	[0.85; 1.00]	< 0.35	No active constraints; normal operation
II	[0.65; 0.85)	[0.35; 0.55)	Minor constraints; improved forecasting recommended
III	[0.45; 0.65)	[0.55; 0.75)	Active constraints; BESS or synthetic inertia required
IV	[0.25; 0.45)	[0.75; 0.90)	Critical threshold; curtailment likely; limiting sub-index identifiable
V	[0.00; 0.25)	> 0.90	Integration infeasible without structural reinforcement

Four physical transitions extracted from the sub-index decomposition anchor the boundaries. At MRID = 0.85 no sub-index is yet restrictive. At 0.65 dynamic constraints begin to degrade while secondary dimensions remain non-critical. At $\mathrm{MRID}_{\mathrm{min}} = 0.45$ standard operational measures such as moderate BESS or curtailment cease to restore secure operation; this same value defines λ^* in (39). At 0.25 the system enters the *dual binding constraint* regime where $H_{\mathrm{eff}} \approx H^{\mathrm{RoCoF}}_{\mathrm{min}}$ and CCT ≈ $\mathrm{CCT}_{\mathrm{ref}}$ coincide, with at least two sub-indices below 0.10 and no isolated operational action capable of recovery. The typical-λ column is an operator-side reference informed by system-operator milestones (EirGrid 2025; Comission 2022; Denholm et al. 2020), not a deterministic mapping.

The normalisation thresholds that produce these boundaries derive from international grid codes published by ENTSO-E and the IEC (ENTSO-E 2022; IEC 2004, 2023a,b, 2024), so recalibrating the index to a specific national framework only requires updating the corresponding sub-index limit without altering the aggregation structure. The IRT classification is determined by the MRID value, while the λ column serves as an operator-oriented reference under standard conditions, since the case-study analysis of Section 7 shows systems sharing the same λ in different IRTs and enabling technologies that shift IRT without changing λ.

5 Spatial Constraint Diagnostics

The aggregate MRID answers *how much* and the limiting sub-index identifies *what*; this section adds the third diagnostic question *where* through the toolkit summarised in Table 4. The four tools target distinct spatial units, share the AC load flow and inertia data used by the aggregate sub-indices, and add no computational cost beyond the values already required by each Φ_k.

Table 4 Spatial diagnostic toolkit embedded in the MRID. Each tool maps an aggregate sub-index onto a specific network unit and answers a distinct *where* question for the operator.

Tool	Spatial unit	Diagnostic question	Linked sub-index
BLI	Branch	Which line is thermally overloaded?	Φ_{HC}
SCR_i	Bus	Which IBR connection point is weakest?	Φ_{GS}
IPF	Generator	Which synchronous unit dominates inertia?	Φ_{IA}, Φ_{NA}
B_{DG}	Network	Does DG siting help the voltage profile?	Φ_{HC}, Φ_{PQ}

5.1 Branch Load Index (BLI)

For each branch l, the branch load index is defined as:

$$\text{BLI}_l(\lambda) = \frac{|S_l(\lambda)|}{S_l^{\max}}, \quad S_l(\lambda) = \sqrt{P_l^2 + Q_l^2} \tag{36}$$

where $S_l(\lambda)$ is the apparent power from the AC load flow and $S_l^{\max}$ is the branch thermal limit. A value $\text{BLI}_l > 1$ indicates a thermally overloaded branch and is the direct cause of Φ_{HC} degradation. The complementary diagnostic role of the BLI is to confirm when the constraint does *not* originate on the branch dimension: a uniformly low BLI_l across the network at a λ where Φ_{HC} is degraded redirects the operator to the voltage dimension at the bus where ΔV_i is binding.

5.2 Per-Bus Short-Circuit Ratio (SCR_i)

The aggregate Φ_{GS} uses the Weighted SCR defined in (34) to capture the system-level grid strength of the renewable fleet. By construction, the WSCR is a power-weighted average, so a low WSCR may signal grid weakness without telling the operator at which bus that weakness is located. The per-bus short-circuit ratio SCR_i, defined in (33), disaggregates the WSCR onto its individual terms and exposes the offending node: the bus with the lowest SCR_i is the weakest connection point and the prime candidate for reactive reinforcement, transformer reconnection or topology redistribution.

This hierarchy makes WSCR and SCR_i complementary rather than redundant. Φ_{GS} enters the geometric mean as a single dimensionless score and answers the system-level question *is the grid strong enough?*; SCR_i answers the spatial question *which bus is weak?*.

5.3 Inertial Participation Factor (IPF)

The inertial participation factor quantifies the relative contribution of each synchronous generator to the total system inertia, identifying the units most critical to frequency stability. It is defined as:

$$\text{IPF}_g(\lambda) = \frac{H_g \cdot S_g^{\text{rated}}}{\sum_{g' \in \mathcal{G}_s} H_{g'} S_{g'}^{\text{rated}}} \tag{37}$$

where H_g is the inertia constant of generator g, S_g^{rated} its rated power, and $\mathcal{G}_s$ the set of synchronous generators in service. Generators with the highest IPF_g are the most critical for sub-indices Φ_{IA} and Φ_{NA}: their disconnection produces the largest reduction in the system equivalent inertia H_{sys}. The IPF can be interpreted as the discrete analogue of the modal participation factor used in small-signal analysis (Gulati 2024; Brahma and Senroy 2021).

5.4 DG Location Benefit Indicator

In radial distribution networks, power injection near loads at the end of a feeder can reduce upstream branch loading and relieve voltage drops along long sections, thereby improving intermediate bus voltage profiles. Under these conditions, increasing renewable penetration λ can actually raise the hosting capacity sub-index Φ_{HC}, locally breaking the MRID monotonicity principle in radial networks.

While Φ_{HC}, computed via the full AC load flow (10), captures this effect implicitly, it does not allow discrimination of which portion of the improvement is attributable to the topological placement of generation, nor which buses are responsible. To provide this diagnostic information, the DG location benefit indicator is defined as:

$$B_{DG}(\lambda) = \frac{1}{N_b} \sum_{i=1}^{N_b} \frac{V_i(\lambda) - V_i(0)}{\Delta V_{\max}} \tag{38}$$

where $V_i(\lambda)$ [pu] is the bus voltage at penetration λ, $V_i(0)$ [pu] is the voltage at the same bus in the baseline case without renewable generation, and $\Delta V_{\max}$ [pu] is the operational voltage band. Positive values indicate that the chosen renewable siting improves the voltage profile relative to the no-DG baseline; negative values indicate that the injection degrades it. The per-bus decomposition $\Delta V_i(\lambda)$ further pinpoints individual nodes where DG is beneficial or detrimental, complementing the BLI information on branch overloads.

The sign of B_{DG} flags whether the chosen IBR siting helps or hurts the voltage profile, complementing the magnitude information already captured by Φ_{HC}.

6 Case Study Configuration and Evaluation Framework

6.1 Test Systems

The MRID behaviour is analysed on the IEEE standard 9-, 14-, 30- and 118-bus test systems (Table 5), widely used as validation benchmarks in the power systems literature (Kundur 1994; Zimmerman et al. 2011).

The four systems span an order of magnitude in installed capacity and cover qualitatively distinct topological regimes, which is the structural diversity required to expose the discriminating capacity of the MRID. The radial or semi-radial nature of the IEEE 9-, 14- and 30-bus systems yields WSCR values typical of weak, rural, island and distributed-generation-dense networks, the operating environments where renewable integration is most challenging (Wang and Milanović 2024; Nedd et al. 2021). Their limited generator count and synchronous inertia H_{sys} in the 4 to 6 s range make their RoCoF and nadir behaviour representative of the high-penetration scenarios projected for the 2030–2040 horizon (Denholm et al. 2020). Their small scale also enables exhaustive scenario and contingency evaluation without sacrificing AC load-flow accuracy or reproducibility (Zimmerman et al. 2011). Networks of comparable size, such as regional and island systems, are typically the first to operate sustained above $\lambda = 0.70$, reinforcing the practical relevance of this benchmark subset.

Table 5 Test systems used for MRID validation. N_b: number of buses; N_l: number of branches.

System	N_b	N_l	P_{load} [MW]	f_0 [Hz]	Role
IEEE 9	9	9	315	60	Weak grid: analytical validation (OMIB)
IEEE 14	14	20	259	60	Weak grid: power flow distribution
IEEE 30	30	41	189	60	Weak grid: topological sensitivity (N-1)
IEEE 118	118	186	4 242	60	Strong grid: large-scale validation

The IEEE 118-bus system contrasts the previous three by introducing a densely meshed transmission topology with 54 synchronous generators and the highest installed capacity in the set. It is representative of strong interconnected systems and serves to assess whether the conclusions drawn from the smaller benchmarks generalise to large-scale infrastructure, where the WSCR is no longer a binding constraint and the dominant limit shifts towards the frequency margin under the largest single contingency.

Table 6 shows the location of renewable sources and BESS storage in the test systems.

Renewable sources (photovoltaic and wind) are modelled by introducing additional injection compensated by a proportional reduction of the dispatch of non-*slack* conventional generators, until a total renewable power of $\lambda \cdot P_{\text{load}}$ is reached. For the IEEE 118-bus system, renewable injection is distributed uniformly among all buses associated with non-*slack* generators, reproducing a distributed penetration scenario. Proportional reduction of conventional dispatch is a conservative criterion that preserves the diversity of

the synchronous fleet and avoids introducing artificial bias in the estimation of system inertia. The effect of renewable injection siting is implicitly captured by the AC load flow and reflected in Φ_{HC}, with spatial decomposition provided by B_{DG} (Section 5.4).

Table 6 Location and characteristics of renewable sources (RES) and BESS storage in the IEEE test systems.

System	RES buses	BESS bus
IEEE 9	5, 6	5
IEEE 14	2, 3, 6	6
IEEE 30	5, 11, 13, 22, 27	13
IEEE 118	non-*slack* generators (53 buses)	80

Synchronous generator inertia constants are assigned by generator size and technology following modern reference values. The IEEE 9-bus fleet, representative of an islanded system with combined-cycle and gas generation, takes $H_1 = 5.0\,\mathrm{s}$ for the 247.5 MV A slack unit, $H_2 = 4.0\,\mathrm{s}$ for the 192 MV A unit and $H_3 = 3.5\,\mathrm{s}$ for the 128 MV A unit. The resulting $H^0_{\mathrm{sys}} \approx 4.3\,\mathrm{s}$ is consistent with insular grids such as the Canary Islands, Ireland or Hawaii. The classical $H_1 = 23.64\,\mathrm{s}$ of (Anderson and Fouad 2003) is a textbook value uncharacteristic of modern power systems and is therefore avoided in this work. The 14-bus and 30-bus fleets use $H \in [2.30, 6.50]\,\mathrm{s}$ and $H \in [2.20, 6.50]\,\mathrm{s}$ respectively, mixing large steam units with hydro and gas turbines. The 118-bus system adopts a size-based assignment $H \in [3.5, 8.5]\,\mathrm{s}$ from 8.5 s for units $\geq 500\,\mathrm{MW}$ down to 3.5 s for units $< 100\,\mathrm{MW}$, yielding $H^0_{\mathrm{sys}} = 6.40\,\mathrm{s}$. Inertia constants are dimensionless and frequency-independent by definition, so the values quoted here apply identically to 50 Hz and 60 Hz systems (Kundur 1994).

The MRID is anchored in ENTSO-E reference limits defined for the Continental European synchronous area at $f_0 = 50\,\mathrm{Hz}$, while the IEEE benchmark systems operate at 60 Hz. Frequency-dependent parameters are translated between the two reference frames according to the physical quantity that the limit is meant to bound. The RoCoF limit translates as a per-unit rate $\dot{f}/f_0$, which is the physically meaningful quantity, yielding $1.2\,\mathrm{Hz\,s^{-1}}$ at 60 Hz for the $1.0\,\mathrm{Hz\,s^{-1}}$ ENTSO-E reference. The nadir limit translates as an absolute deviation from nominal, so the European 49.0 Hz floor becomes 59.0 Hz, preserving the same 1 Hz admissible drop. The quasi-steady-state deviation $\Delta f_{\max} = 0.2\,\mathrm{Hz}$ is invariant under either interpretation and is used directly. The reference clearing time is the only parameter that is not derived by scaling: $\mathrm{CCT}_{\mathrm{ref}} = 0.250\,\mathrm{s}$ corresponds to the typical maximum back-up protection actuation time for modern transmission relays, a hardware characteristic that does not scale with nominal frequency. Table 7 summarises the correspondence between ENTSO-E references and the values used in this study.

Table 7 Frequency parameters: ENTSO-E reference values at 50 Hz and scaled equivalents at 60 Hz used in this study. The emergency nadir row is included as the regulatory load-shedding threshold for reference and does not enter the Φ_{NA} formulation, which uses only the operational nadir limit $f_{\mathrm{nadir,min}}$.

Parameter	50 Hz	60 Hz	Translation rule
Max RoCoF $\dot{f}_{\max}$	$1.0\,\mathrm{Hz\,s^{-1}}$	$1.2\,\mathrm{Hz\,s^{-1}}$	Same $\dot{f}/f_0$ in pu/s
Min nadir $f_{\mathrm{nadir,min}}$	49 Hz	59 Hz	Same absolute drop 1 Hz
Emergency nadir	47.5 Hz	57.5 Hz	Same absolute drop 2.5 Hz
$\mathrm{CCT}_{\mathrm{ref}}$	0.150 s	0.250 s	Hardware-bound, no frequency scaling
QSS dev. $\Delta f_{\max}$	0.2 Hz	0.2 Hz	Frequency-invariant by definition

6.2 Penetration Scenarios

A set of 20 penetration levels, $\lambda \in [0.05, 1.00]$ with step $\Delta\lambda = 0.05$, is evaluated in the main sweep via AC Newton-Raphson load flow (MATPOWER) (Zimmerman et al. 2025). The sweep covers the five Integration Regime Types defined in Section 4 and extends deliberately beyond the currently admissible operational envelope. The upper end of the range is therefore not a feasibility region but a controlled extrapolation: it allows the MRID curves to reveal how each system continues degrading past the IRT-IV/V boundary and identifies the asymptotic binding constraints that would govern a fully renewable instantaneous regime. Without this overshoot, the four qualitatively distinct limiting mechanisms documented in

Section 7 would not separate clearly at the upper end of the sweep.

Parametric analyses requiring a fixed operating point use the reference level $\lambda_{\text{ref}} = 0.65$, which lies at the centre of IRT-III and matches the 2025 EirGrid/SONI SNSP target (EirGrid 2025; Nedd et al. 2021). The active curtailment study is the only exception, being conducted at $\lambda = 0.80$, where curtailment becomes operationally relevant while the hosting-capacity margin Φ_{HC} remains sufficient.

6.3 Evaluation Framework

The baseline characterisation consists of sweeping MRID(λ) over each of the four IEEE systems using the reference generation fleet and no enabling technologies. Building on this baseline, the validation of the MRID is structured as a set of targeted evaluations designed to demonstrate its discriminating capability, physical interpretability, and robustness.

6.3.1 Evaluation 1: Discriminating capacity

The diagnostic question is whether two systems with identical scalar penetration (λ_P) can belong to different integration regimes, a distinction that unidimensional metrics cannot capture by construction.

To produce reproducible results, a factorial design samples the four IEEE systems at three penetration levels spanning the operational window, $\lambda \in \{0.45, 0.65, 0.80\}$. For each combination, seven cases represent plausible operator-side perturbations:

- ***A*** standard reference configuration.
- ***B*** severe low-inertia variant, $H_f \times 0.20$, probing the dynamic backbone of the system.
- ***C*** doubled-impedance variant, $Z_f \times 2$, probing network strength.
- ***D*** intermediate low-inertia variant, $H_f \times 0.50$, complementing case B.
- ***E*** reference with BESS at 15 % of load, which corresponds to the central sample of the BESS sweep $P_{\text{BESS}} \in \{0, 0.05, 0.15, 0.30\}$ used later in the technology-enablers study and provides cross-study comparability.
- ***F*** full grid-forming fleet ($k_{\text{GFM}} = 1.00$).
- ***G*** added synchronous condenser, representing the main families of enabling technologies.

The resulting 84 scenarios target two diagnostic properties: first, whether systems indistinguishable under scalar metrics are separated into different Integration Regime Types by the MRID; and second, whether the spatial diagnostic toolkit of Section 5 identifies the specific network elements responsible for this separation. Each scenario is consequently reported through three readings in series: the aggregate MRID and its IRT (*how much*), the limiting sub-index Φ_k (*what*) and the spatial signature BLI/SCR$_i$/IPF/B_{DG} that pinpoints the responsible network element (*where*). Together these establish whether the MRID can substitute scalar penetration metrics in planning workflows.

6.3.2 Evaluation 2: Technology enablers and limits

The diagnostic question shifts from *can we separate* to *can we predict what works*: given the dominant constraint identified in the baseline characterisation, this evaluation tests whether the MRID can anticipate which enabling technologies effectively unlock additional integration capacity.

Two complementary sweeps are used. The first explores inverter-based interventions in the $k_{\text{GFM}} \times P_{\text{BESS}}$ plane, with $k_{\text{GFM}} \in \{0, 0.30, 1.00\}$ and $P_{\text{BESS}} \in \{0, 0.05, 0.15, 0.30\}\, P_{\text{load}}$, covering the range of currently planned operational deployments. The second examines active renewable curtailment through a sweep of $\kappa \in [0, 0.50]$ at $\lambda = 0.80$, where curtailment becomes operationally relevant while Φ_{HC} still retains margin below λ_{ref}.

These surfaces additionally provide the local sensitivities $\partial\text{MRID}/\partial P_{\text{BESS}}$ and the asymptotic synthetic-inertia ceiling without requiring separate experiments. The outcome of this evaluation is the ability to determine, prior to deployment, in which regimes each technology increases admissible integration and in which it does not alter the limiting constraint.

6.3.3 Evaluation 3: Robustness and uncertainty

The final question is whether the diagnostic conclusions remain valid under the three perturbation

classes a planning-grade index must withstand: subjective weight assignment, topological N-1 contingencies, and parametric uncertainty in inertia and impedance. Three complementary sweeps address each class.

Sweep 3.1 computes a normalised weight tornado, evaluating $\partial \mathrm{MRID}/\partial w_k$ at $\lambda = \lambda_{\mathrm{ref}}$ under $\pm\delta w = \pm 0.10$, corresponding to the level of disagreement typically observed in Analytic Hierarchy Process (AHP) elicitation.

Sweep 3.2 performs a complete branch-by-branch N-1 contingency analysis at five penetration levels, recording the base, worst-case, and median MRID for each system, thereby exposing the topological dependence of the operational margin.

Sweep 3.3 executes a Monte Carlo simulation with $N = 500$ realisations per system. The sampling distributions are $\lambda \sim \mathcal{U}[0.10, 0.90]$, $H_f \sim \log\mathcal{N}(0,\, 0.35)$ truncated to $[0.20,\, 2.00]$, and $Z_f \sim \log\mathcal{N}(0,\, 0.25)$ truncated to $[0.50,\, 2.50]$. The same Monte Carlo framework benchmarks the full MRID against an electromechanical-restricted baseline $\mathrm{MRID}_{\mathrm{em}}$, defined as the geometric mean over the subset $\{\Phi_{IA}, \Phi_{TS}, \Phi_{NA}\}$ with renormalised weights. The discrepancy between $\mathrm{MRID}_{\mathrm{em}}$ and MRID across the sample isolates the contribution of Φ_{HC}, Φ_{FR}, Φ_{PQ}, and Φ_{GS}, quantifying the diagnostic information added beyond the electromechanical domain, particularly in systems where the binding constraint lies outside this subspace.

7 Results

This section organises the results around the structure introduced in Section 6. Subsection 7.1 presents the baseline characterisation $\mathrm{MRID}(\lambda)$ on the four IEEE systems, the maximum admissible penetration on each, the sub-index decomposition and the integration-regime maps. Subsections 7.2, 7.3 and 7.4 report Evaluations 1, 2 and 3 respectively.

7.1 Baseline characterisation

This subsection presents the baseline $\mathrm{MRID}(\lambda)$ on the four IEEE systems under the reference fleet and no enabling technologies. The reading proceeds in three steps: the maximum admissible penetration λ^*, the sub-index decomposition that identifies the binding constraint on each benchmark, and the limiting-mechanism map that links every benchmark to the canonical reading of the literature.

The boundary $\mathrm{MRID}_{\min} = 0.45$ defined in Table 3 separates admissible from inadmissible integration. The maximum admissible penetration level is therefore

$$\lambda^* = \sup\Big\{\lambda \in [0,1] \;\Big|\; \mathrm{MRID}(\lambda, \boldsymbol{\xi}) \geq \mathrm{MRID}_{\min}\Big\} \tag{39}$$

Figure 1 shows the $\mathrm{MRID}(\lambda)$ curves of the four systems under default weights and identifies λ^* graphically as the crossing point with $\mathrm{MRID}_{\min}$.

The four values, taken at the largest λ of the $\Delta\lambda = 0.05$ sweep that still satisfies $\mathrm{MRID} \geq \mathrm{MRID}_{\min}$, are $\lambda^*_9 = 0.70$, $\lambda^*_{14} = \lambda^*_{30} = 0.80$ and $\lambda^*_{118} = 0.85$. The ordering reflects the structural strength of each system: the small insular IEEE-9 with $H^0_{\mathrm{sys}} = 4.32\,\mathrm{s}$ saturates first, the mid-sized IEEE-14 and IEEE-30 hold the same ceiling, and the densely meshed IEEE-118 with $H^0_{\mathrm{sys}} = 6.40\,\mathrm{s}$ admits the highest penetration. Figure 1 traces $\mathrm{MRID}(\lambda)$ for each system overlaid with the limiting-mechanism band.

The sub-index decomposition assigns each benchmark to the constraint family the literature has long associated with it. The IEEE 9-bus system, the canonical reference for transient-stability and frequency studies (Anderson and Fouad 2003; Kundur 1994), is bound by Φ_{NA} throughout the admissible range, with Φ_{IA} as the secondary binding dimension; the frequency-stability framing matches the textbook reading of this benchmark. The IEEE 14-bus system, designed as an OPF benchmark and known for the three synchronous condensers at buses 3, 6 and 8 that provide its reactive backbone, binds on Φ_{HC} from $\lambda = 0.05$ with a structural voltage floor at 0.27, and on Φ_{GS} at higher penetrations. This dual binding is the IBR-aware reading of the same voltage-support deficit the literature has long documented for this system. The IEEE 30-bus system, repeatedly identified in voltage-stability studies as constrained by weak buses with documented reactive needs, binds on Φ_{GS} from $\lambda \approx 0.20$, with the bus-level diagnostic pinpointing bus 5 as the weakest connection point precisely where the literature locates the canonical weak nodes. The IEEE 118-bus system, the standard reference for studies of strong

meshed networks and frequency response under large disturbances (Athay et al. 1979; University of Washington), binds on Φ_{NA} while Φ_{GS} remains at unity throughout the admissible range, indicating that the limit is set by the largest N-1 contingency rather than by local grid strength, exactly as the literature predicts.

Both IEEE-9 and IEEE-14 exhibit a mild non-monotonic rebound of Φ_{HC} in the high-penetration tail, the same effect formally analysed in Section 5.4: dense IBR injection at radial load buses or at buses adjacent to reactive-support units lifts local voltages and partially relieves average voltage violations. The geometric aggregation absorbs this rebound because the binding sub-indices Φ_{NA} and Φ_{GS} keep degrading faster, and the aggregate MRID(λ) remains strictly decreasing as required by principle P5, which constrains only the aggregate and admits this kind of local sub-index rebound by construction.

For planning purposes, each benchmark calls for a different family of remedies, the one its binding constraint demands. The 9-bus needs inertia restoration, the 14- and 30-bus systems need reactive support at the IBR connection points, and the 118-bus needs containment of the largest contingency. Section 7.3 extends this picture by mapping how λ^* evolves under combinations of grid-forming inverter fraction k_{GFM} and BESS capacity, quantifying how much each remedy unlocks the admissible range in each system.

7.2 Evaluation 1: Discriminating capacity

This subsection answers whether systems with identical scalar penetration occupy the same integration regime and, if not, which network element drives the separation. The 84 scenarios decide both questions simultaneously: the aggregate MRID and its limiting Φ_k resolve *how much* and *what*, while the spatial layer of Section 5 closes the loop with *where*.

Figure 2 concentrates the evidence at the central penetration $\lambda = 0.65$ for the seven cases of every system, reporting the MRID, the dominant sub-index and the IRT achieved. Table 8 extends the same readings to the boundary penetrations $\lambda = 0.45$ and $\lambda = 0.80$ and identifies, for each system, the case that drives the largest deviation from the reference configuration.

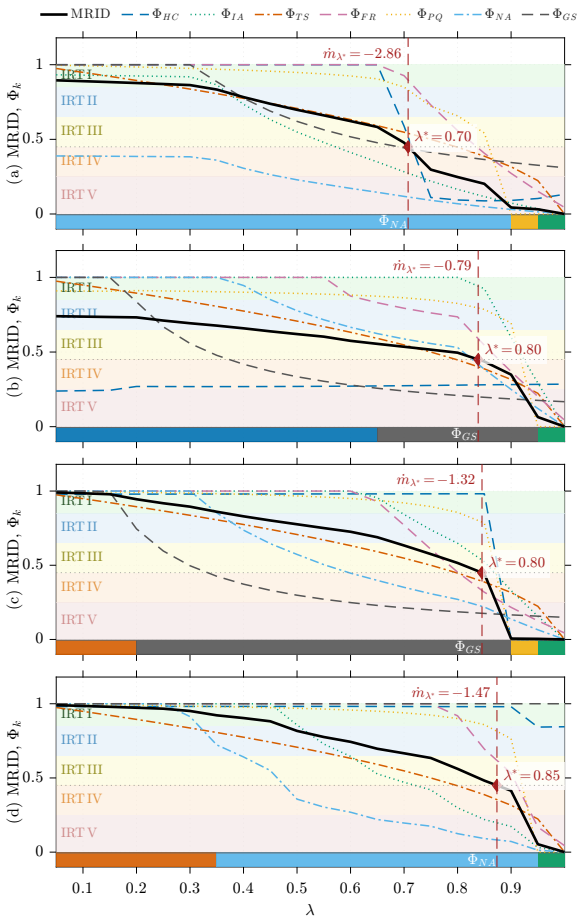

Fig. 1 Limiting mechanism map and sub-index evolution for the four IEEE systems. Panels: **(a)** IEEE 9-bus, **(b)** IEEE 14-bus, **(c)** IEEE 30-bus, **(d)** IEEE 118-bus. Each panel shows MRID(λ) in black overlaid with the seven $\Phi_k(\lambda)$ in colours; the strip below each panel identifies, at each λ, the sub-index with the lowest value, and the diamond marker locates λ^* annotated with the local slope $\dot{m}_{\lambda^*}$.

Three planning-relevant readings emerge from this central group. First, the qualifier *high penetration* becomes system- and configuration-dependent: every system spans two or three Integration Regime Types at $\lambda = 0.65$ despite the seven cases sharing the same λ_P, λ_C and SNSP value, with ranges II–IV (9-bus), III–IV (14-bus), II–IV (30-bus) and I–III (118-bus). The operational reading is that a regulatory or contractual statement of the form *operate at or below* $\lambda = 0.65$ remains silent on whether the system is structurally safe or one configuration change away from

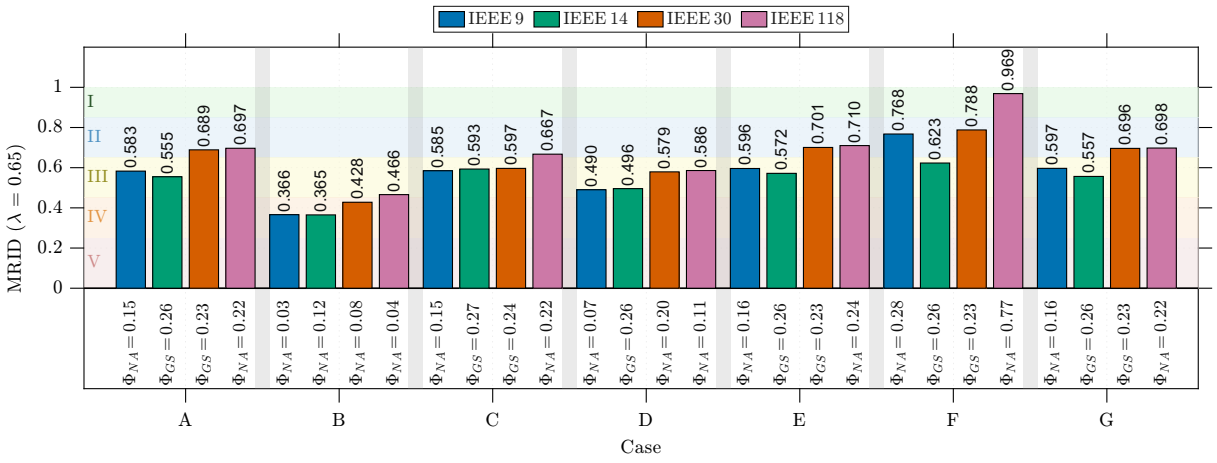

Fig. 2 Evaluation 1 at $\lambda = 0.65$: MRID, IRT classification and dominant sub-index Φ_k for the seven cases A–G across the four IEEE systems.

infeasibility, and the MRID is what closes that gap.

Table 8 Evaluation 1. IRT coverage and MRID span across the seven cases A–G for each system at $\lambda = 0.45$ and $\lambda = 0.80$, including the case achieving the largest deviation relative to the reference configuration.

	$\lambda = 0.45$		$\lambda = 0.80$		
System	**IRTs**	**MRID span**	**IRTs**	**MRID span**	**Case for max. IRT shift**
9-bus	I–III	0.395	IV–V	0.401	F (V → IV at λ=0.80)
14-bus	II–IV	0.255	III–IV	0.280	B (III → IV at λ=0.65)
30-bus	I–III	0.329	II–IV	0.340	B (II → IV at λ=0.65, 2 IRTs)
118-bus	I–III	0.373	I–IV	0.572	F (III → I at λ=0.80, 2 IRTs)

Second, the binding physical mechanism is primarily a system property and only secondarily a function of the configuration. The 9- and 118-bus systems remain bound by Φ_{NA} across the seven cases A–G, the 14- and 30-bus systems by Φ_{GS} in every case except the low-inertia variants B and D, where Φ_{NA} takes over. This stability of the binding family confirms the system-level expert diagnoses summarised in the baseline characterisation: dynamic perturbations such as inertia reduction can substitute one frequency-related dimension for another, but they do not relocate a structurally voltage- or strength-limited system into the frequency-binding regime.

Third, the GFM full fleet of case F is the most efficient single lever, but its efficacy depends primarily on the spatial dispersion of IBR injection. Case F lifts IEEE-118 by two IRTs at $\lambda = 0.80$, from III to I with MRID = 0.947, because virtual inertia is distributed across 53 IBR buses and recovers the frequency margin almost completely. By contrast, on the 9-bus system, with only two IBR buses, case F gains a single IRT at every penetration level and at $\lambda = 0.80$ leaves the system in IRT-IV with MRID = 0.401. The 14- and 30-bus systems, bound by grid strength, remain essentially unaffected under case F at high λ. This shows that GFM is necessary but not sufficient, and the index identifies the exception before the deployment.

The spatial layer of Section 5 adds the network-element identity behind each separation. Table 9 reports, for the reference configuration of each system at $\lambda = 0.65$, the most loaded branch via the BLI, the weakest IBR bus via SCR_i, the most critical synchronous generator via the IPF and the sign of the DG location benefit via B_{DG}. Figure 3 retains the IEEE-9 BLI heat map as a concrete reading of how the BLI pattern behaves across the seven cases A–G: no branch saturates, the most loaded corridor is the 6–7 line at BLI ≈ 0.66, and the cases that modify the generator fleet leave the pattern essentially unchanged. The

weak-grid variant of case C with $Z \times 2$ perturbs the loading distribution upwards but stays within thermal limits, evidence that the Φ_{NA} binding of the IEEE-9 system originates on the dynamic dimension and not on branch overload.

Table 9 Evaluation 1. Spatial signature of the reference configuration (case A) for each test system at $\lambda = 0.65$: branch with maximum BLI, IBR bus with minimum SCR_i, synchronous generator with maximum IPF, and DG location benefit indicator B_{DG}.

Metric	9-bus	14-bus	30-bus	118-bus
BLI max (branch)	0.665 (6–7)	0.833 (1–2)	1.079 (6–8)	0.833 (19–20)
SCR_i min (bus)	1.43 (bus 6)	0.73 (bus 6)	0.67 (bus 5)	4.40 (bus 87)
IPF max (gen)	0.504 (gen 1)	0.895 (gen 1)	0.665 (gen 1)	0.107 (gen 30)
B_{DG}	+0.082	−0.016	+0.031	+0.008

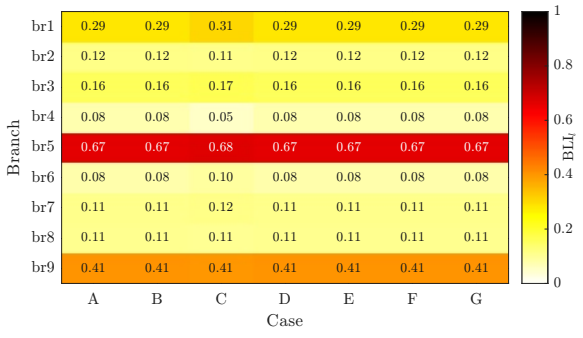

Fig. 3 Branch Load Index BLI_l per branch (rows) and case A–G (columns) for the IEEE 9-bus system at $\lambda = 0.65$. Branch 1–4 concentrates the highest loading in all cases without reaching thermal saturation; cases B, D–G preserve the reference distribution and only case C (weak grid, $Z \times 2$) shifts the loading pattern.

Four spatial readings emerge from Table 9 and sharpen the discriminating message of the aggregate MRID by pointing to the same network elements the literature has independently flagged. First, the BLI exposes the only configuration that exceeds thermal capacity in the reference case: IEEE-30 reaches $\mathrm{BLI}_{6\text{-}8} = 1.079$ at $\lambda = 0.65$, locating the corridor that documented weak-bus studies identify as central to the reactive bottleneck of this benchmark. The remaining three systems stay below saturation. Second, the per-bus SCR_i aligns with documented weak buses: bus 5 in IEEE-30 ($\mathrm{SCR}_5 = 0.67$) is one of the three weakest nodes catalogued in the voltage-stability literature, bus 6 in IEEE-14 ($\mathrm{SCR}_6 = 0.73$) is the location of one of the three synchronous condensers of the system, and bus 87 in IEEE-118 ($\mathrm{SCR}_{87} = 4.40$) remains above the IEC 61400-21 minimum, consistent with the meshed-network framing of that benchmark. Third, the IPF spans two orders of magnitude across systems. At the high end, $\mathrm{IPF}_1 = 0.895$ in IEEE-14 reflects that one unit carries 90 % of the system inertia, so its disconnection becomes the dominant frequency contingency. At the low end, $\mathrm{IPF}_{\max} = 0.107$ in IEEE-118 means that no single generator controls the frequency margin. Fourth, B_{DG} is positive and small across all four systems, with values in $[-0.016, +0.082]$, indicating that the chosen IBR siting at the documented gen and weak-bus locations is approximately neutral on the voltage profile, with a marginal positive contribution on the 9-bus only. The same nominal λ under the same reference configuration thus produces four different lists of network-level actions: branch reinforcement on the 6–8 corridor of IEEE-30, reactive reinforcement at bus 6 of IEEE-14 and bus 5 of IEEE-30, contingency hardening on the slack units of IEEE-9 and IEEE-14, and operational margin extension on the largest contingency for IEEE-118.

The extension to the boundary penetrations of Table 8 reinforces the same diagnostic under more stress. At $\lambda = 0.45$ the discriminating capacity is widest on the strongest systems: IEEE-118 spans I–III with a MRID spread of 0.373 between case F and the low-inertia case B, and IEEE-30 spans I–III with 0.329. At $\lambda = 0.80$ the spread peaks on the system most amenable to inverter-side intervention: IEEE-118 covers I–IV with a record MRID spread of 0.572, driven by case F lifting the system from III to I, while IEEE-9 falls to IRT-V in every case except the inverter-based ones E and F, confirming that the small insular fleet has run out of operational margin at that penetration level. In summary, the discriminating capacity of the MRID grows where the operating envelope is widest and the remedies more numerous, and collapses into a narrow band when the system is too small or too stressed to be saved by the seven test interventions.

7.3 Evaluation 2: Technology enablers and limits

This subsection answers whether the MRID can anticipate, before deployment, which technology investment unlocks integration capacity in each benchmark and which does not. The two sweeps reported here, the $k_{\mathrm{GFM}} \times P_{\mathrm{BESS}}$ map of λ^* and the curtailment trace, quantify this anticipation.

Table 10 reports λ^* for each combination of system, k_{GFM} and $P_{\mathrm{BESS}}/P_{\mathrm{load}}$, and Figure 4 traces the corresponding MRID(λ) curves with the λ^* markers superimposed. Within Table 10, the $k_{\mathrm{GFM}} = 0$ row yields the local sensitivity $\partial\mathrm{MRID}/\partial P_{\mathrm{BESS}}$ and the saturation of λ^* along P_{BESS} exposes the asymptotic ceiling of synthetic-inertia compensation.

The $k_{\mathrm{GFM}} \times P_{\mathrm{BESS}}$ sweep orders the four systems on a continuous gradient of response to GFM that the spatial distribution of IBR siting predicts. The IEEE 118-bus system, with its 53 IBR buses, gains the most: λ^* rises from 0.85 at $k_{\mathrm{GFM}} = 0$ to 1.00 with $k_{\mathrm{GFM}} = 0.30$ and BESS at 5 % of load. Distributed virtual inertia recovers the frequency margin nearly completely. The IEEE 14-bus system, with three IBR buses, gains the second most: λ^* rises from 0.80 to 1.00 with full GFM and BESS at 15 %. The IEEE 30-bus saturates at $\lambda^* = 0.85$ regardless of k_{GFM}: its binding constraint Φ_{GS} is structural and is not relieved by inverter control. The IEEE 9-bus, with only two concentrated IBR buses, also exhibits negligible improvement: full GFM and BESS at 15 % only raises λ^* from 0.70 to 0.75. The implication is that GFM efficacy scales with IBR dispersion when the binding is frequency-related and is essentially neutral when the binding is grid strength, a conditionality that the MRID emits before any device is procured.

Active renewable curtailment is examined at $\lambda = 0.80$, the level at which the action becomes operationally relevant. Table 11 reports the MRID and the IRT before and after applying $\kappa = 0.20$, plus the dominant Φ_k on each side of the action.

Table 10 Evaluation 2. Maximum admissible penetration λ^* per system and combination of GFM fraction k_{GFM} and BESS capacity $P_{\mathrm{BESS}}/P_{\mathrm{load}}$.

		$P_{\mathrm{BESS}}/P_{\mathrm{load}}$			
System	k_{GFM}	**0**	0.05	0.15	0.30
9-bus	0.00	0.70	0.70	0.70	0.70
	0.30	0.70	0.70	0.70	0.70
	1.00	0.70	0.70	0.75	0.75
14-bus	0.00	0.80	0.80	0.85	0.85
	0.30	0.85	0.90	0.90	0.90
	1.00	0.95	0.95	1.00	1.00
30-bus	0.00	0.80	0.85	0.85	0.85
	0.30	0.85	0.85	0.85	0.85
	1.00	0.85	0.85	0.85	0.85
118-bus	0.00	0.85	0.85	0.85	0.90
	0.30	0.95	1.00	1.00	1.00
	1.00	1.00	1.00	1.00	1.00

The same nominal curtailment $\kappa = 0.20$ at $\lambda = 0.80$ has very different efficacy across the four systems, ordered by the operational proximity of each to its IRT-V boundary. The largest gain is in IEEE-9, the most stressed system at this penetration: curtailment lifts the MRID from 0.248 in IRT-V to 0.591 in IRT-III, a recovery of +0.343 index units that crosses two regime boundaries while Φ_{NA} remains the binding constraint, indicating that the relief is propagated through all dimensions but anchored on the same frequency bottleneck. The IEEE 30-bus system gains +0.184 from IRT-III to IRT-II with Φ_{GS} persisting as binding before and after the action. The IEEE 118-bus, already in IRT-III at $\lambda = 0.80$, gains +0.142 to reach IRT-II under the same Φ_{NA} binding family. The IEEE 14-bus, structurally pinned by Φ_{GS} at low values, exhibits negligible improvement of only +0.063 and stays in IRT-III: curtailment does not relieve the IBR grid-strength bottleneck because reducing the injection per IBR bus is bounded by the few buses concentrating it. In summary, curtailment is most cost-effective on systems that are both close to their IRT-V boundary and frequency-bound, and least effective on systems whose binding is structurally rooted in the IBR siting itself.

Table 11 Evaluation 2. Curtailment effect at $\lambda = 0.80$ with $\kappa = 0.20$, equivalent to an effective penetration $\lambda(1-\kappa) = 0.64$: MRID, IRT and dominant Φ_k before and after the action across the IEEE test systems.

	κ=0			κ=0.20			
System	**MRID**	**IRT**	**Limiting Φ_k**	**MRID**	**IRT**	**Limiting Φ_k**	**ΔMRID**
IEEE 9	0.248	V	$\Phi_{NA} = 0.069$	0.591	III	$\Phi_{NA} = 0.150$	+0.343
IEEE 14	0.496	III	$\Phi_{GS} = 0.209$	0.559	III	$\Phi_{GS} = 0.261$	+0.063
IEEE 30	0.516	III	$\Phi_{GS} = 0.186$	0.699	II	$\Phi_{GS} = 0.233$	+0.184
IEEE 118	0.561	III	$\Phi_{NA} = 0.125$	0.703	II	$\Phi_{NA} = 0.225$	+0.142

7.4 Evaluation 3: Robustness and uncertainty

This subsection answers whether the diagnostic conclusions survive three independent perturbations: weight assignment (C1), topological N-1 contingencies (C2) and parametric uncertainty in inertia and impedance (C3). The block additionally benchmarks the MRID against the electromechanical-restricted baseline MRID_{em} to isolate the irreducible information the MRID adds beyond a frequency-only framework.

The baseline against which the MRID is benchmarked in subexperiment C3 is constructed from the same formulation as the MRID itself, restricted to the electromechanical sub-set $\{\Phi_{IA}, \Phi_{TS}, \Phi_{NA}\}$ with weights renormalised to unity:

$$\text{MRID}_{\text{em}} = \prod_{k \in \{IA,TS,NA\}} \Phi_k^{w_k^\dagger} \qquad w_k^\dagger = \frac{w_k}{w_{IA} + w_{TS} + w_{NA}} \tag{40}$$

By construction, MRID_{em} omits Φ_{HC}, Φ_{FR}, Φ_{PQ} and Φ_{GS} and represents the diagnostic information available to a framework focused exclusively on frequency-domain dynamics. The discrepancy between MRID_{em} and MRID across the Monte Carlo sample isolates the dimensions in which the MRID adds irreducible information.

Table 12 reports $\partial\text{MRID}/\partial w_k$ for each sub-index across the four systems at $\lambda = \lambda_{\text{ref}}$ under $\pm\delta w = \pm 0.10$. The analytical identity $\partial\text{MRID}/\partial w_k = \text{MRID} \cdot \ln(\Phi_k)$ predicts the sign: the sensitivity is negative when Φ_k is below the global MRID and positive otherwise, so the tornado doubles as an active-constraint detector.

Table 12 Evaluation 3.1. Normalised weight sensitivity $\partial\text{MRID}/\partial w_k$ per system at $\lambda = \lambda_{\text{ref}} = 0.65$ under $\pm\delta w = \pm 0.10$. Negative entries identify the binding sub-indices ($\Phi_k < \text{MRID}_{\text{base}}$); their magnitudes quantify how much each binding constraint dominates the global index.

	9-bus	**14-bus**	**30-bus**	**118-bus**
w_{HC}	+0.423	−0.474	+0.343	+0.305
w_{IA}	−0.294	+0.368	+0.322	−0.201
w_{TS}	+0.065	+0.028	−0.063	−0.107
w_{FR}	+0.423	+0.247	+0.299	+0.320
w_{PQ}	+0.341	+0.267	+0.295	+0.266
w_{NA}	−0.841	+0.058	−0.360	−0.865
w_{GS}	−0.075	−0.486	−0.780	+0.306

The pattern recovers the binding family identified in the baseline through an independent computation: w_{NA} is the most negative sensitivity on IEEE-9 (−0.841) and IEEE-118 (−0.865), confirming the frequency-binding diagnosis; w_{GS} is the most negative on IEEE-30 (−0.780) and on IEEE-14 (−0.486, jointly with w_{HC} at −0.474), confirming the grid-strength binding documented in the spatial diagnostics. The IRT classification at $\lambda = \lambda_{\text{ref}}$ is preserved under ± 0.10 weight perturbations in all four systems, indicating that the diagnosis is robust to the weight elicitation method and that the tornado functions simultaneously as a robustness check and as an automated detector of the dominant constraint.

The complete branch-by-branch N-1 sweep was executed on the four IEEE systems at five penetration levels. The graphical comparison in Figure 6 is restricted to IEEE-30 and IEEE-118 because the IEEE-9 and IEEE-14 systems do not provide statistically robust N-1 samples; their data are still reported in Table 13.

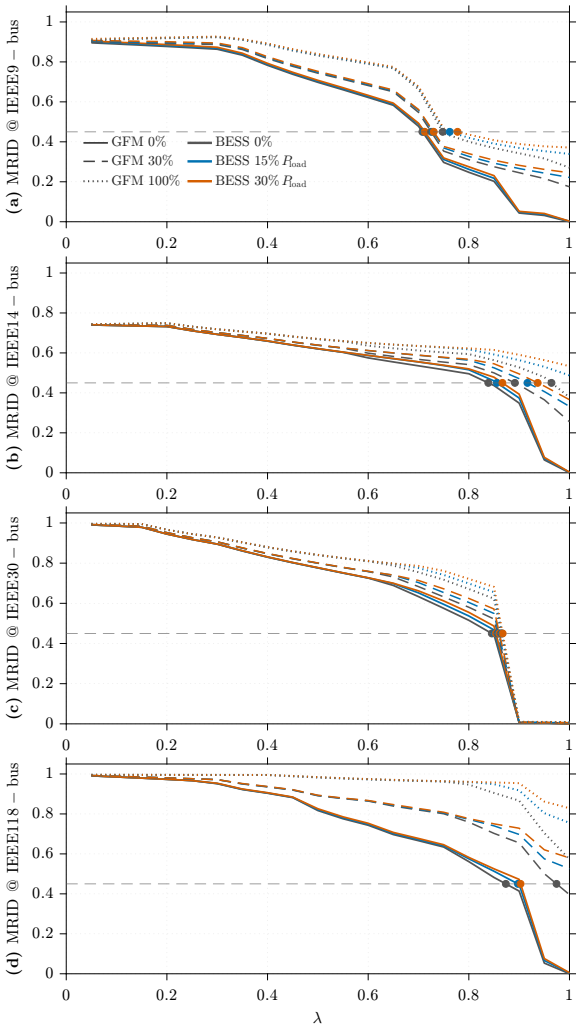

Fig. 4 Evaluation 2. MRID(λ) for the four IEEE systems under combinations of k_{GFM} and P_{BESS}. Markers indicate λ^* for each configuration.

Table 13 Evaluation 3.2. Maximum base-to-worst-N-1 gap (% of the $[0, 1]$ index range) and the λ at which it occurs, plus the mean base-to-median gap, for the four IEEE systems.

	9-bus	**14-bus**	**30-bus**	**118-bus**
Branches	9	20	41	186
Max worst-case gap	35.9%	6.3%	11.8%	3.2%
λ at max	0.35	0.20	0.20	0.20
Mean median gap	−0.24%	−0.02%	+0.12%	+0.00%

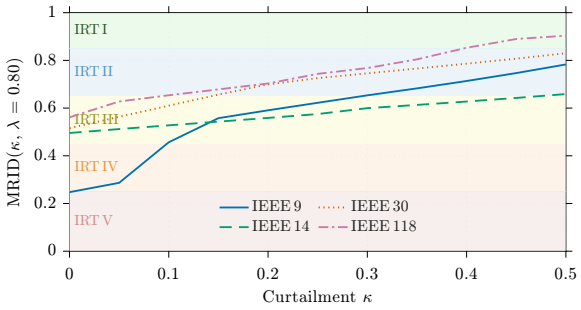

Fig. 5 Evaluation 2. MRID(κ) at $\lambda = 0.80$ for the four IEEE systems.

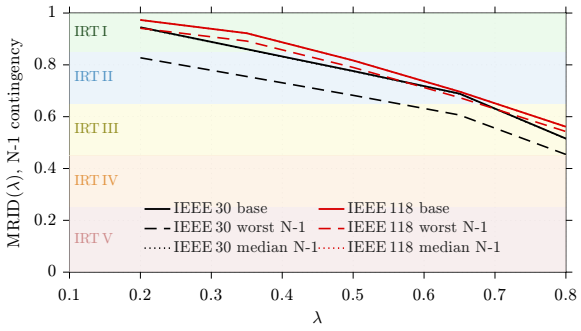

Fig. 6 Evaluation 3.2. MRID(λ) under base, worst-case-N-1 and median-N-1 conditions for IEEE-30 (black) and IEEE-118 (red).

The N-1 statistics separate the four systems along the topological-redundancy axis. IEEE-9, with only 9 branches and minimal redundancy, exhibits the largest base-to-worst gap of 35.9% of the index range at $\lambda = 0.35$: a single line outage can erase a third of the operational margin. IEEE-30 shows a moderate gap of 11.8% at low λ. IEEE-118, densely meshed with 186 branches, contains the maximum gap to 3.2% and the mean median gap to zero, indicating that contingency-induced degradation is absorbed by the network. Two systems landing at the same value of MRID(λ) can therefore exhibit substantially different operational reliability under N-1, as the 35.9% gap on IEEE-9 demonstrates, and the MRID paired with the worst-case curve produces a contingency-aware admissibility ceiling rather than a single-point one.

$N = 500$ realisations per system explore the joint distribution of MRID and $\mathrm{MRID}_{\mathrm{em}}$ under $\lambda \sim \mathcal{U}[0.10, 0.90]$ and lognormal perturbations of

inertia and impedance. Table 14 reports the correlations and the fraction of discordant scenarios per system, defined as $\mathrm{MRID}_{\mathrm{em}} > 0.75$ combined with $\mathrm{MRID} < 0.65$, the regime in which the electromechanical-restricted baseline declares the system acceptable while the full MRID detects a relevant constraint outside the electromechanical sub-set.

Table 14 Evaluation 3.3. Monte Carlo correlations ρ, r_s between MRID and $\mathrm{MRID}_{\mathrm{em}}$, valid sample size, fraction of discordant scenarios per system, and the dominant sub-index responsible for the discordance.

	9-bus	**14-bus**	**30-bus**	**118-bus**
N_{valid}	497	500	498	500
Pearson ρ	0.9595	0.9384	0.9497	0.9893
Spearman r_s	0.9938	0.9277	0.9924	0.9982
Discordant	0.0%	23.0%	0.0%	0.0%
Φ_k in discords.	—	Φ_{HC}/Φ_{GS}	—	—

The reading is quantitative: the irreducible information the MRID adds over an electromechanical-only framework concentrates on the systems whose binding constraint falls outside that subset. IEEE-9 and IEEE-118, bound by Φ_{NA} (a sub-index already present in $\mathrm{MRID}_{\mathrm{em}}$), correlate almost perfectly with the baseline ($\rho \geq 0.96$, $r_s \geq 0.99$, zero discordants); IEEE-30, bound by Φ_{GS} but with Φ_{NA} moving alongside the rest of the trajectory, produces zero discordants under the chosen threshold. IEEE-14, bound jointly by Φ_{HC} and Φ_{GS}, surfaces 23.0% of discordant scenarios, with 82 % of those discordances driven by Φ_{HC} and 18 % by Φ_{GS}. The MRID identifies these structurally voltage- and strength-bound situations as inadmissible while the electromechanical baseline declares them acceptable, and the magnitude of this disagreement quantifies the diagnostic value added by the MRID beyond a frequency-only framework.

7.5 Use of the MRID as a planning cost function

The differentiability of all seven sub-indices makes the aggregate MRID directly usable as the objective function of the planning maximisation problem

$$\max_{\boldsymbol{u}} \ \mathrm{MRID}(\lambda, \boldsymbol{\xi}(\boldsymbol{u})) \tag{41}$$

with control vector

$$\boldsymbol{u} = [P_{\mathrm{BESS}},\, \mathrm{SoC}_{\mathrm{BESS}},\, \tau_{\mathrm{BESS}},\, P_{\mathrm{curt}},\, Q_{\mathrm{comp}},\, \boldsymbol{P}_g^{\mathrm{disp}},\, \boldsymbol{u}_{\mathrm{IBR}}]^T$$

where $\boldsymbol{u}_{\mathrm{IBR}} = [k_{\mathrm{GFM}},\, H_{\mathrm{GFM}},\, k_{\mathrm{cond}}]^T$ collects the inverter-related decisions. The discrete sweeps of Evaluations 1 and 2 can be replaced by closed-form remedy selection through the chain rule on (6), which yields the gradient of the aggregate index with respect to any control variable u_j:

$$\frac{\partial \mathrm{MRID}}{\partial u_j} = \sum_{k \in \mathcal{K}} w_k \, \frac{\mathrm{MRID}}{\Phi_k} \, \frac{\partial \Phi_k}{\partial u_j} \tag{42}$$

This expression weights each sub-index contribution by the ratio MRID/Φ_k, so the binding sub-index dominates the gradient as long as $\Phi_k \ll \mathrm{MRID}$. Two contrasting benchmarks of Evaluation 2 illustrate the behaviour of this gradient as an MPC dispatcher.

On the IEEE 118-bus system at the upper end of its admissible range, the binding Φ_{NA} produces the largest partial derivative with respect to k_{GFM} among the available controls, recovering in closed form the same dominant action that the discrete sweep of Table 10 reaches by exhaustive search. On the IEEE 30-bus system, the binding Φ_{GS} yields a near-zero sensitivity to both k_{GFM} and P_{BESS}, correctly predicting that no inverter-side intervention unlocks integration capacity and that the operator must consider structural remedies at the weak buses identified by the spatial diagnostics. The gradient therefore returns zero for the available controls and signals the need to extend the control vector before any operational improvement is achievable.

These two cases illustrate how the MRID used as an MPC cost function automates the regime-aware remedy selection that the discrete evaluations of Section 7.3 produce, at the cost of a single AC load flow per gradient evaluation.

8 Discussion and Conclusions

The baseline characterisation and three thematic evaluations of Section 7 converge on a single validation argument from four independent paths: the baseline characterisation identifies the binding constraint of each benchmark via the sub-index

decomposition, Evaluation 1 confirms it across 84 plausible configurations, Evaluation 2 shows how each remedy class interacts with that constraint, and Evaluation 3 reproduces the same binding under weight, topological and parametric perturbation. Achieved without case-specific tuning, this convergence is the case-study basis for applying the MRID to systems where comparable expert intuition has not been built.

The MRID is formulated as a planned-operation hosting-capacity index, not as a post-fault reconfigurability index. The contingencies that enter Φ_{HC}, Φ_{IA}, Φ_{TS} and Φ_{NA} are severity scenarios used to size the per-sub-index margin, not the state in which the index is evaluated. Whether a system can keep operating at the same penetration after a contingency has materialised lies outside the present scope and is among the natural extensions listed below.

The case-study analysis on the four IEEE benchmarks yields four conclusions of direct operational relevance.

1. **A network-anchored regime classification from scalar penetration.** The MRID separates configurations indistinguishable under λ_P, λ_C or SNSP into distinct Integration Regime Types, and its embedded spatial diagnostic layer of BLI, SCR_i, IPF and B_{DG} pinpoints the branch, bus or generator that drives each separation. The qualitative shorthand *high renewable penetration* is thereby replaced by an operationally actionable state with a network address on which the operator can act.
2. **A priori prediction of enabling-technology efficacy.** From the same AC load-flow data, the MRID discriminates which systems gain integration capacity from BESS and grid-forming inverters and which remain pinned by structural grid-strength deficits, and identifies which physical deficit each curtailment level addresses. Investment decisions previously made by trial-and-error become regime-specific prescriptions issued before any device is procured.
3. **Single-computation recovery of canonical expert intuition.** Applied without case-specific calibration, the MRID returns on each IEEE benchmark the binding mechanism that the literature has converged upon through decades of independent study: Φ_{NA} on the frequency-limited IEEE-9 and IEEE-118, Φ_{HC} together with Φ_{GS} on the voltage-support-limited IEEE-14, and Φ_{GS} at the documented weak buses of IEEE-30. The spatial layer recovers the very network elements that the literature flags as critical, including bus 5 of IEEE-30 and the synchronous-condenser bus 6 of IEEE-14. The index thus collapses a distributed body of expert analysis into a single computation, providing the case-study basis for extending the diagnosis to systems where comparable intuition has not been built.
4. **Diagnosis robust to elicitation, topology, and modelling scope.** The MRID IRT classification is invariant to ± 0.10 weight perturbations, and the tornado independently recovers the same binding constraint. The branch-by-branch N-1 sweep exposes a topological dependence of the operational margin that single-point scores hide: the small insular IEEE-9 loses up to 35.9 % of the index range to a single line outage, while the meshed IEEE-118 stays below 3.2 %. The Monte Carlo benchmark against an electromechanical-restricted baseline isolates Φ_{HC} and Φ_{GS} as information that the MRID adds beyond stability-based frameworks, with 23 % of discordant scenarios on IEEE-14.

Beyond its diagnostic role, the MRID is directly usable as the cost function of a planning maximisation problem, demonstrated on two contrasting IEEE benchmarks in Section 7.5 where the closed-form gradient recovers the dispatch decisions that the discrete sweeps of Evaluation 2 produce by exhaustive search, at the cost of a single AC load flow per gradient evaluation. The operational consequence is that planning decisions previously reliant on qualitative judgement can be grounded on a reproducible computation: the AC load flow already in routine use produces a regime classification, the binding sub-index, the responsible network element, and the gradient directions to act on. The open-source implementation on the four IEEE benchmarks establishes a verifiable baseline against which future multidimensional renewable integration indices can be compared on equal terms.

The present formulation is deliberately confined to what can be computed from a single AC load flow per evaluation, the constraint that gives the diagnosis its planning-tractability and reproducibility. Several natural extensions emerge when this constraint is relaxed, each adding a modelling layer outside the present scope. Replacing the analytical CCT in Φ_{TS} with a SIME surrogate trained on time-domain simulations would raise stability fidelity at the cost of departing from the load-flow paradigm. Per-inverter-type recalibration of $\mathrm{SCR}_{\mathrm{ref}}$ in Φ_{GS} is a refinement that the IEC reference value already approximates at the system level. Applying the framework to active distribution networks calls for a meshed-grid reformulation of Φ_{GS} and an adaptation of the spatial diagnostic layer to radial topologies. Extending the probabilistic block of subexperiment 3.3 to hidden Markov chains over IRT-state sequences lifts the snapshot index into a temporal trajectory suitable for long-term stochastic planning. Enriching the spatial diagnostic toolkit with modal-participation metrics (Gulati 2024; Brahma and Senroy 2021) would require eigendecomposition of the linearised dynamic system, complementing the load-flow-derived BLI, SCR_i, IPF and B_{DG} already embedded in the present formulation.

Declarations

Funding

This research received no external funding.

Conflict of interest

The authors declare no competing financial or non-financial interests.

Consent for publication

All authors have read and approved the final manuscript and consent to its publication.

Code availability

The MATLAB simulation scripts used to produce all results reported in this paper are publicly available at https://doi.org/XXXX (Zenodo repository, DOI to be confirmed upon publication). The repository contains the simulation routines (`run_discriminating.m`, `run_technology.m`, `run_robustness.m`, `run_montecarlo.m`) together with the corresponding MATPOWER (Zimmerman et al. 2025) data files for the IEEE 9-, 14-, 30- and 118-bus test systems.

Author contributions

N. Moreno-Alfonso: conceptualisation, mathematical formulation, MATLAB implementation, writing—original draft. J.C. Bravo-Rodríguez: supervision, methodological review. A. Bachiller-Soler: supervision, methodological review.

References

AEMO: Engineering Roadmap to 100% Renewables (2022). https://www.aemo.com.au/-/media/files/initiatives/engineering-framework/2022/engineering-roadmap-to-100-per-cent-renewables.pdf Accessed 2026-05-04

Anderson, P.M., Fouad, A.A.: Power System Control and Stability, (2003)

Adetokun, B.B., Ojo, J.O., Muriithi, C.M.: Reactive power-voltage-based voltage instability sensitivity indices for power grid with increasing renewable energy penetration. IEEE access : practical innovations, open solutions **8**, 85401–85410 (2020) https://doi.org/10.1109/ACCESS.2020.2992194

Athay, T., Podmore, R., Virmani, S.: A Practical Method for the Direct Analysis of Transient Stability. IEEE Transactions on Power Apparatus and Systems **PAS-98**(2), 573–584 (1979) https://doi.org/10.1109/TPAS.1979.319407

Alizadeh, M., Sun, W.: Dynamic Interactions Between Inverter-Based Resources and Synchronous Generators: A Comparative Study for Cascading Failure Risk. IEEE Access **13**, 102830–102847 (2025) https://doi.org/10.1109/ACCESS.2025.3579293

Benzerga, A., Bahmanyar, A., Derval, G., Ernst, D.: A Unified Definition of Hosting Capacity, Applications, and Review. IEEE Access

13, 7819–7836 (2025) https://doi.org/10.1109/ACCESS.2024.3521223

Bai, X., Fan, Y., Hou, J., Liu, J.: Evaluation method of renewable energy flexibility confidence capacity under different penetration rates. Energy **281**, 128327 (2023) https://doi.org/10.1016/j.energy.2023.128327

Brahma, D., Senroy, N.: Spatial Distribution of Grid Inertia and Dynamic Flexibility: Approximations and Applications. IEEE Transactions on Power Systems **36**(4), 3465–3474 (2021) https://doi.org/10.1109/TPWRS.2021.3050085

Beyza, J., Yusta, J.M.: The effects of the high penetration of renewable energies on the reliability and vulnerability of interconnected electric power systems. Reliability Engineering & System Safety **215**, 107881 (2021) https://doi.org/10.1016/j.ress.2021.107881

Cai, Y., Gong, Z., Huang, W., Zhou, Y.: Rapid Estimation of CCT for GFM and GFL Inverters Integrated Systems Using the Direct Method. In: 2024 IEEE 8th Conference on Energy Internet and Energy System Integration (EI2), pp. 948–953 (2024). https://doi.org/10.1109/EI264398.2024.10991892

Comission, E.: REPowerEU Plan (2022). https://eur-lex.europa.eu/resource.html?uri=cellar:fc930f14-d7ae-11ec-a95f-01aa75ed71a1.0001.02/DOC_1&format=PDF Accessed 2026-05-04

Denholm, P., Mai, T., Kenyon, R.W., Kroposki, B., O'Malley, M.: Inertia and the power grid: A guide without the spin. NREL Technical Report TP-6A20-73856 (2020) https://doi.org/10.2172/1659820

EC: COMMISSION REGULATION (EU) 2016/631 of 14 April 2016 Establishing a Network Code on Requirements for Grid Connection of Generators (2016)

EirGrid: System Non-Synchronous Penetration. Calculation Update (2025). https://cms.eirgrid.ie/sites/default/files/publications/SNSP_Calculation_Update_V1.0_EirGrid.pdf Accessed 2026-04-08

Energinet: Fast Frequency Reserve – Solution to the Nordic inertia challenge. Technical report (2019). https://energinet.dk/media/r4hbaom5/ffr-ig-justification-report.pdf Accessed 2026-05-04

ENTSO-E: Inertia and Rate of Change of Frequency (RoCoF). Technical report. https://eepublicdownloads.entsoe.eu/clean-documents/SOC%20documents/Inertia%20and%20RoCoF_v17_clean.pdf Accessed 2026-05-04

ENTSO-E: Frequency stability evaluation criteria for the synchronous zone of continental europe. Technical report, ENTSO-E (2022). https://www.entsoe.eu

ESO, N.G.: National Trends and Insights. Technical report (2021). https://www.neso.energy/document/190151/download Accessed 2026-05-04

El Wejhani, S., Tnani, S., Elleuch, M., Ben Kilani, K., Ennine, G.: Stability indices in power networks: A correlation–regression analysis for renewable energy integration. Electrical Engineering **107**(10), 13501–13517 (2025) https://doi.org/10.1007/s00202-025-03221-5

Gulati, A.: A Novel Approach for Dynamic Analysis of Wind-Integrated Multi-Machine Power Systems. Journal of Electrical Systems **20**(3), 1287–1298 (2024) https://doi.org/10.52783/jes.3536

IEC: IEC 61727:2004 Photovoltaic (PV) Systems. Characteristics of the Utility Interface (2004)

IEC: IEC 61400-21: Wind Energy Generation Systems (2023)

IEC: IEC 62898 Microgrids (2023)

IEC: IEC 62933 Electrical Energy Storage (EES) Systems (2024)

Keane, A., O'Malley, M.: Optimal allocation of embedded generation on distribution networks. IEEE Transactions on Power Systems

20(3), 1640–1646 (2005) https://doi.org/10.1109/TPWRS.2005.852115

Kundur, P.: Power System Stability and Control. McGraw-Hill, New York (1994)

Liu, X., Fang, X., Gao, N., Yuan, H., Hoke, A., Wu, H., Tan, J.: Frequency Nadir Constrained Unit Commitment for High Renewable Penetration Island Power Systems. IEEE Open Access Journal of Power and Energy **11**, 141–153 (2024) https://doi.org/10.1109/OAJPE.2024.3370504

Milano, F., Dörfler, F., Hug, G., Hill, D.J., Verbič, G.: Foundations and challenges of low-inertia systems. Power Systems Computation Conference (PSCC) (2018) https://doi.org/10.23919/PSCC.2018.8450880

Milanović, J.V.: Probabilistic stability analysis: The way forward for stability analysis of sustainable power systems. Philosophical Transactions of the Royal Society A: Mathematical, Physical and Engineering Sciences **375**(2100), 20160296 (2017) https://doi.org/10.1098/rsta.2016.0296

Mousa, H.H.H., Mahmoud, K., Lehtonen, M.: A Comprehensive Review on Recent Developments of Hosting Capacity Estimation and Optimization for Active Distribution Networks. IEEE Access **12**, 18545–18593 (2024) https://doi.org/10.1109/ACCESS.2024.3359431

Nedd, M., Bukhsh, W., MacIver, C., Bell, K.: Metrics for determining the frequency stability limits of a power system: A GB case study. Electric Power Systems Research **190**, 106553 (2021) https://doi.org/10.1016/j.epsr.2020.106553

NERC: Integrating Inverter- Based Resources into Low Short Circuit Strength Systems. Reliability Guideline. Technical report, North American Electric Reliability Corporation (2017). https://www.nerc.com/comm/PC/InverterBased%20Resource%20Task%20Force%20IRPTF/IRPTF_WhitePaper_11-08-17.pdf Accessed 2026-04-13

Nikolaidis, A.I., Gonzalez-Longatt, F.M., Charalambous, C.A.: Indices to Assess the Integration of Renewable Energy Resources on Transmission Systems. Conference Papers in Science **2013**(1), 324562 (2013) https://doi.org/10.1155/2013/324562

Nejla, E., Saidani, K., Besbes, M.: Overcoming the integration bottleneck: A global review of renewable energy and grid adaptation strategies. International Journal of Sustainable Energy **44**(1), 2569922 (2025) https://doi.org/10.1080/14786451.2025.2569922

Niu, S., Zhang, Z., Ke, X., Zhang, G., Huo, C., Qin, B.: Impact of renewable energy penetration rate on power system transient voltage stability. Energy Reports **8**, 487–492 (2022) https://doi.org/10.1016/j.egyr.2021.11.160

Ochoa, L.F., Padilha-Feltrin, A., Harrison, G.P.: Evaluating distributed generation impacts with a multiobjective index. IEEE Transactions on Power Delivery **21**(3), 1452–1458 (2006) https://doi.org/10.1109/TPWRD.2005.860262

Papadopoulos, P.N., Milanović, J.V.: Probabilistic Framework for Transient Stability Assessment of Power Systems With High Penetration of Renewable Generation. IEEE Transactions on Power Systems **32**(4), 3078–3088 (2017) https://doi.org/10.1109/TPWRS.2016.2630799

Ríos-Ocampo, J.P., Arango-Aramburo, S., Larsen, E.R.: Renewable energy penetration and energy security in electricity markets. International Journal of Energy Research **45**(12), 17767–17783 (2021) https://doi.org/10.1002/er.6897

Ratnam, K.S., Palanisamy, K., Yang, G.: Future low-inertia power systems: Requirements, issues, and solutions. Renewable and Sustainable Energy Reviews **124**, 109773 (2020) https://doi.org/10.1016/j.rser.2020.109773

Rosso, R., Wang, X., Liserre, M., Lu, X., Engelken, S.: Grid-forming converters: Control approaches, grid-synchronization, and future trends. IEEE Open Journal of Industry Applications **2**, 93–109 (2021) https://doi.org/10.

1109/OJIA.2021.3074028

Strelkov, M., Strelkova, H.: Penetration of renewable energy in the infrastructural system of the electricity market. 2020 IEEE 7th international conference on energy smart systems (2020) https://doi.org/10.1109/ESS50319.2020.9160221

Teng, F., Aunedi, M., Strbac, G.: Benefits of flexibility from smart electrified transportation and heating in the future UK electricity system. Applied Energy **167**, 420–431 (2016) https://doi.org/10.1016/j.apenergy.2015.10.028

University of Washington: Power System Test Case Archive. 118 Bus. University of Washington. https://labs.ece.uw.edu/pstca/pf118/pg_tca118bus.htm Accessed 2026-05-14

Wang, M., Milanović, J.V.: Simultaneous Assessment of Multiple Aspects of Stability of Power Systems With Renewable Generation. IEEE Transactions on Power Systems **39**(1), 97–106 (2024) https://doi.org/10.1109/TPWRS.2023.3241862

Yang, B., Chatterjee, D., Johnson, B., Seo, G.-S.: Transient Stability Analysis Framework for Grid-Forming Inverter-Dominated Networks Under Large Grid Disturbances. In: 2025 IEEE Energy Conversion Conference Congress and Exposition (ECCE), pp. 1–8 (2025). https://doi.org/10.1109/ECCE58356.2025.11260192

Yu, B., Fang, D., Yu, H., Zhao, C.: Temporal-spatial determinants of renewable energy penetration in electricity production: Evidence from EU countries. Renewable Energy **180**, 438–451 (2021) https://doi.org/10.1016/j.renene.2021.08.079

Zimmerman, R.D., Murillo-Sanchez, C.E., Gan, D.: MATPOWER (Version 8.1) (2025). https://doi.org/10.5281/zenodo.15871662

Zimmerman, R.D., Murillo-Sánchez, C.E., Thomas, R.J.: MATPOWER: Steady-State Operations, Planning, and Analysis Tools for Power Systems Research and Education. IEEE Transactions on Power Systems **26**(1), 12–19 (2011) https://doi.org/10.1109/TPWRS.2010.2051168